Colloids and Surfaces A: Physicochemical and Engineering Aspects 622 (2021) 126648

Contents lists available at ScienceDirect

Colloids and Surfaces A: Physicochemical and Engineering Aspects

journal homepage: www.elsevier.com/locate/colsurfa

GRGDS-conjugated and curcumin-loaded magnetic polymeric nanoparticles for the hyperthermia treatment of glioblastoma cells

Fatih Senturk [a,1], Soner Cakmak [b,*], Ismail Cengiz Kocum [c], Menemse Gumusderelioglu [b], Goknur Guler Ozturk [a]

[a] Department of Biophysics, Faculty of Medicine, Gazi University, Ankara, Turkey
[b] Division of Bioengineering, Graduate School of Science and Engineering, Hacettepe University, Ankara, Turkey
[c] Department of Biomedical Engineering, Baskent University, Ankara, Turkey

HIGHLIGHTS

- Dual encapsulation of SPIONs and curcumin in polymeric nanoparticles (Cur-m-PNPs).
- GRGDS conjugation to Cur-m-PNPs reduced cytotoxic dose of free curcumin by 2.5-fold.
- Multifunctional m-PNPs showed effective heating performance under AC magnetic field.
- High therapeutic efficacy in T98G cells was achieved *via* multifunctional m-PNP induced hyperthermia.

GRAPHICAL ABSTRACT

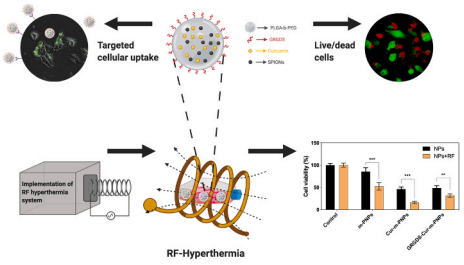

ARTICLE INFO

Keywords:
Glioblastoma
RF hyperthermia
GRGDS
Curcumin
Magnetic nanoparticles

ABSTRACT

Thermally responsive and ligand-mediated drug delivery systems have the potential to improve the treatment of brain tumors, especially, most lethal one, glioblastoma multiform (GBM). Magnetic nanoparticle-mediated hyperthermia becomes one of the most promising alternative therapy for GBM treatment in cases where localized heating and targeted delivery of a therapeutic drug can be achieved on the tumor site. In this study, it is aimed to increase the therapeutic efficiency of multi-functionalized nanoparticles (NPs) in combination with radio-frequency hyperthermia (RF-HT) on GBM cells. For this purpose, firstly, a low-cost and portable home-built RF-HT system suitable for *in vitro/in vivo* studies was successfully implemented and tested at 13.56 MHz frequency with power up to approximately 400 W. Subsequently, the highly monodispersed superparamagnetic iron oxide nanoparticles (SPIONs), which could interact with the RF magnetic field, were synthesized with the mean particle size of 5.6 ± 0.9 nm. The obtained SPIONs were coated with poly (lactic-co-glycolic acid)-poly (ethylene glycol) di-block copolymer (PLGA-b-PEG). Most of the SPIONs were uniformly distributed in such a well-defined spherical-shaped polymeric NP. Moreover, curcumin (Cur), a potential agent for GBM treatment, was loaded into the magnetic polymeric nanoparticles (m-PNPs) with a loading capacity of 8% (w/w, Cur/NPs) and a mean diameter of Cur-loaded m-PNPs (Cur-m-PNPs) was 142 ± 70 nm. To increase cellular uptake and targeting ability of NPs, glycine-arginine-glycine-aspartic acid-serine (GRGDS) peptide was immobilized on the Cur-m-PNPs and the amount of GRGDS was detected as 37 μg/mg NPs. *In vitro* cytotoxicity studies revealed that the presence of GRGDS on Cur-m-PNPs (GRGDS-Cur-m-PNPs) improved the cytotoxic efficiency of Cur-m-PNPs by 6-fold in GBM

* Corresponding author.
E-mail address: scakmak@hacettepe.edu.tr (S. Cakmak).
[1] Present address: Department of Biophysics, Faculty of Medicine, Duzce University, Duzce, Turkey.

https://doi.org/10.1016/j.colsurfa.2021.126648
Received 8 February 2021; Received in revised form 8 April 2021; Accepted 10 April 2021
Available online 15 April 2021

cells for all incubation times (24, 48 and 72 h). Furthermore, NPs with RF treatment exhibited higher antitumor activity than that of NPs without RF on GBM cells. This result may be attributed to the thermal (SPIONs) or non-thermal (cellular membrane) effects or both of them on cells. Overall, this study showed that RF-HT in combination with GRGDS-Cur-m-PNPs could provide a feasible approach to improve GBM treatment.

1. Introduction

Glioblastoma multiforme (GBM) is one of the deadliest primary brain tumors in adults, most patients do not survive further than a year, and only 5% stay alive beyond 5 years [1]. There are many factors for this poor prognosis of GBM, most of the difficulties are its histopathological situation such as high intrusive-angiogenic character [2], the high drug resistance of GBM, and the presence of the blood-brain barrier (BBB) which limits the penetration of drugs in the tumor region [3,4]. Current treatment options of newly diagnosed GBM are comprised of maximal safe surgical resection followed by radiotherapy and adjuvant, as well as concomitant temozolomide (TMZ) since 2005 [5]. While TMZ therapy has increased overall survival (OS) from 12.1 to 14.6 months, tumor recurrence invariably occurs and TMZ resistance remains one of the major challenges [3–5].

Although GBM has the lowest median OS among all malignant brain tumors, there have been some improvements in the treatment of GBM by using the biological effect in the radiofrequency (RF) region of the electromagnetic (EM) spectrum. Tumor-treating fields (TTFields, Novocure Inc, Israel), which is designed by focusing on the direct-biological effects of RF, use 200 kHz alternating-electric fields that interfere with dividing cancer cells [6], induce cell cycle arrest and apoptosis in the glioblastoma cells [7]. Stupp et al. reported that OS was significantly prolonged by 4.9 months with TMZ+TTFields compared to TMZ alone in newly diagnosed GBM patients [8]. In addition to TTFields, hyperthermia is considered as an alternative method for cancer therapy that also uses the -direct or -mediated biological effects of RF fields. In hyperthermia therapy, the tissue is induced by an intentional increase in temperature that either destroys the tissue or renders the cancer cells more vulnerable against chemo-radio therapy [9]. However, magnetic nano hyperthermia depends on the idea that magnetic nanoparticles delivered to tumors can increase temperature after exposure to an external magnetic field and eventually induce cell death [10].

The unique magnetic properties of superparamagnetic iron oxide nanoparticles (SPIONs), which renders them susceptible to the external magnetic field [11,12], have received tremendous attention for GBM treatments [13]. Superparamagnetic iron oxide nanoparticles can be synthesized by different methods such as co-precipitation, thermal decomposition, microemulsion, sol-gel and etc. [14]. Among the others, low-cost co-precipitation and high-temperature thermal decomposition are the most common methods used to synthesize SPIONs. While low-cost and simple production is the best-known advantages of co-precipitation, this method has some drawbacks such as broad size distribution and high agglomeration of SPIONs [15]. On the other hand, highly monodisperse SPIONs can be effectively synthesized by thermal decomposition method [14].

It has been reported that the combination of magnetic nano hyperthermia with radiotherapy, which is approved for the treatment of recurrent GBM in Europe, increased OS by 7.2 months compared to standard TMZ treatments [2]. Although many clinical trials have been carried out to improve the effectiveness of GBM treatment, the success criteria of trials were reported that the increase of only several months in overall survival of patients. In addition, among treatment-associated severe adverse events, reduced neurologic function and negative impact on the quality of life are observed in patients. Therefore, more effective novel therapeutic agents or strategies are needed to improve GBM treatment. Moreover, many alternative molecules have been investigated whereas curcumin has been reported as one of the most effective potential candidates for GBM treatment [3].

Curcumin (Cur) is one of the natural pharmaceutical compounds that accumulate in the hippocampus by passing the blood-brain barrier, and its lipophilic nature provides appropriate absorption to the central nervous system [16]. Curcumin has become a potential drug for glioblastoma [3] and inhibits cell proliferation *via* various molecular and cellular signaling pathways concurrently in cytoplasm and nucleus in glioblastoma cells [17]. There are many preclinical studies of Cur indicating that it was used as an effective anti-tumor agent against GBM, or curcumin application before chemotherapy could make patients more sensitive to the treatment [18]. However, poor bioavailability and low solubility of Cur in aqueous media limit its therapeutic applications [19–21]. In order to overcome these limitations, nanocarriers have been developed with certain functions, providing important advantages such as overcoming physiological barriers and increasing the water solubility and circulation time of curcumin [22].

Many different polymers, such as poly (lactic-co-glycolic acid) (PLGA), polyethylene glycol (PEG), and polyvinyl alcohol (PVA) have been investigated as nanocarriers to enhance the poor solubility and retention time of curcumin in aqueous media. Among them, PLGA is attracting more attention due to its unique properties such as biocompatibility, biodegradability, efficient intracellular endocytosis, and FDA approval [23]. Also, PEG is one of the most widely used polymers because of its ability to escape recognition by the immune system, prevent macrophage attachment, and enhance retention time for drug delivery studies [24]. In recent years, many studies have been carried out to improve the targeting of Cur-loaded polymeric NPs (Cur-PNPs) on various cancer cells [25]. In some disease states (especially cancer), specific receptors are over-expressed, and receptor-mediated transport (RMT) utilizes this feature for the active targeting of nanoparticles [26]. For this purpose, depending on the type of cancer cells, suitable ligands such as monoclonal antibody [27], folic acid [28] and arginine-glycine-aspartic acid (RGD) [29] have been conjugated to Cur-PNPs for active targeting of NPs. RGD has been regarded as one of the high binding affinity to integrins that over-expressed on the vasculature of tumor microenvironments and also GBM cells [30]. In addition, conjugation of the glycine-arginine-glycine-aspartic acid-serine (GRGDS) to the NPs has been shown to increase cellular uptake of the GBM cells [31]. Therefore, we focused on GRGDS as a promising ligand because this peptide has selective affinity for the $\alpha_v\beta_3/\alpha_v\beta_5$ integrins that are overexpressed on the GBM cells [31,32].

Several researchers have investigated the antitumor efficiency of magnetic nano hyperthermia treated with Cur-SPIONs co-loaded into exosome [3], dendrimer [28], liposome [33] and ß-cyclodextrin [34] on cancer cell lines. Most of the magnetic nano hyperthermia studies mediated with SPIONs have been used at the band of frequency up to 1 MHz, however, there were only a few studies at the frequency of 13.56 MHz, and targeting-ligands were not used in these studies [35, 36]. Also, the frequency of 13.56 MHz not only increases the temperature but also affects the electrical properties of the cell membrane [37]. It is widely known that RF hyperthermia (RF-HT, 13.56 MHz) has a thermal-killing effect on cells which is regarded as the major working mechanism [38]. However, the possible non-thermal effect of RF-HT, largely disregarded by most researchers, was approved especially in the cell membrane bilayer [39]. This interaction between the cell membrane and RF may change the ionic gradient of the membrane, thus RF creates an additional non-thermal effect related to ion fluxes. RF-hyperthermia has thermal and non-thermal effects, and both effects can create a synergic effect [38]. These effects may increase the cellular uptake that leads to enhanced therapeutic efficiency of nanocarriers.

Additionally, 13.56 MHz RF frequency has been approved for clinical cancer treatment in Europe [40]. It should be noted that RF-HT may have increased the cellular uptake of NPs by changing electrophysiological activity within the cell membrane [40]. Also, RF-HT has been used to effectively render cancer cells more sensitive before chemotherapy [25], this enhanced chemo-sensitivity after RF treatment may be related to the more cellular uptake and also RF-membrane non-thermal interaction, as well as thermal effect, contributed to this enhanced therapeutic efficiency.

According to the published literature, there is no report on 13.56 MHz RF-magnetic field in combination with GRGDS-conjugated and curcumin-loaded magnetic polymeric nanoparticles (GRGDS-Cur-m-PNPs) for improving targeting therapeutic efficiency on the T98G glioblastoma cell lines. For this purpose, in this study, it is aimed to implement an efficient RF hyperthermia system in the frequency of medical band to increase cell death with the functionalized nanoparticles which display thermal effects with RF-SPIONs interactions, non-thermal effects with RF-cell membrane interactions, anti-proliferative effects with curcumin, and targeting potential with GRGDS on T98G cells.

2. Materials and methods

2.1. Materials

Iron (III) chloride hexahydrate ($\geq$ 99%), Iron (II) chloride tetrahydrate ($\geq$ 99%), sodium oleate (95%), 1-octadecene (90%), oleic acid (90%), poly(lactic-co-glycolic acid) (PLGA) (lactide:glycolide, 50:50, Mw:30000–60000), poly(ethylene glycol) 2-aminoethyl ether acetic acid (COOH-PEG-NH_2, Mn:3500), 1-ethyl-3-(3-dimethyl-aminopropyl) carbodiimide (EDC), N-hydroxysuccinimide sodium salt (NHS), dimethyl formamide (DMF, $\geq$ 99%), dichloromethane (DCM), polyvinyl alcohol (PVA), acetonitrile (HPLC grade), curcumin (Mw: 368.38 Da with purity $\geq$ 65%), ammonium hydroxide (NH_4OH, 25%), hydrochloric acid (HCl, 37%), hexane and dimethyl sulfoxide (DMSO) were purchased from Sigma-Aldrich, Germany. All other chemicals were obtained from Sigma-Aldrich unless specifically mentioned otherwise.

2.2. RF-hyperthermia system

Magnetic hyperthermia experiments were carried out using a home-built radiofrequency (RF) hyperthermia system that consists of an RF oscillator, RF driver, RF amplifier, RF impedance-matching network, induction coil applicator (solenoid and pancake geometry), water cooling system, and a thermal camera (Scheme S1 and Fig. S1). RF driver (AN779L) and amplifier (EB104) (disassembly circuits) in kit forms designed by Motorola company were purchased from Communication Concepts Inc. (USA) and these component sets were assembled by the manufacturer instructions with slight modification (manual of AN779L-EB104). In addition, all of the RF equipment was properly tested before and after the assembly process with the applicable testing equipment (multimeter, signal generator, oscilloscope, dummy load, inductance-capacitance (LC) meter, etc.). Thereafter, the impedance matching network was implemented to prevent damage against reflected power causing a dramatic increase in temperature at the junctions of power transistors in the RF driver-amplifier system. A standing wave ratio power-meter (SWR and dummy load, ME-165/G, USA) was also used to measure this forward/reflected power of the RF signal. Aluminum boxes were made to prevent interference in electronic devices and/or to prevent the employee from being affected by high power RF-fields. After that, water-cooled coils with two different geometry (solenoid and pancake) were built to generate a magnetic field, and these applicators were integrated into an RF system for *in vitro* cell culture studies.

2.3. Synthesis of superparamagnetic iron oxide nanoparticles

Superparamagnetic iron oxide nanoparticles (SPIONs) were synthesized by the thermal decomposition method with some minor modifications [41]. For iron-oleate complex synthesis, 10.8 g iron (III) chloride and 36.5 g sodium oleate were dissolved in a mixture composed of ethanol (80 mL), ultrapure water (60 mL), and hexane (140 mL). The final solution was heated to 70 °C and kept at this temperature for 4 h. After the reaction was completed, the solution of the iron-oleate complex was washed three times with ultrapure water in a separatory funnel and dried in a vacuum. For monodisperse iron oxide nanoparticle synthesis; 36 g of iron-oleate complex and 5.7 g of oleic acid (OA) were mixed in 200 g of 1-octadecene by mechanical stirring under an argon atmosphere. The mixture was heated to 320 °C at a heating rate of 3–4 °C/min and kept at that temperature for 30 min. The final suspension was then cooled to room temperature and an equal volume of ethanol was added to precipitate the nanoparticles. Then, the nanoparticles were washed several times with ethanol to remove any excess surfactants by centrifugation and neodymium magnet. Finally, SPIONs were dispersed in hexane and stored at 4 °C.

2.4. Synthesis of PLGA-b-PEG di-block copolymer

Di-block copolymers of poly (lactic-co-glycolic acid) (PLGA) and poly (ethylene glycol) (PEG) were synthesized using EDC-NHS chemistry [42]. In brief, 100 mg of PLGA was dissolved in 20 mL of DMF with gentle stirring and then, activated with 1172.2 μM NHS and 1198.3 μM EDC. This solution was allowed to react overnight at room temperature. The resulting PLGA-NHS was washed in ice-cold methanol by three times to discard non-reacted EDC-NHS and dried in a vacuum. The activated PLGA-NHS (80 mg) was dissolved in 4 mL DMF, and then, reacted with 26.6 μM hetero bi-functional PEG (COOH-PEG-NH_2) with average Mn:3500. This mixture was incubated for 12 h at room temperature with gentle stirring. The obtained PLGA-b-PEG di-block copolymer was washed in ice-cold methanol by three times to remove non-reacted PEG and dried in a vacuum at room temperature before further use. PLGA-b-PEG copolymer was characterized for molecular weight and polydispersity by gel permeation chromatography (Omnisec GPC/SEC system, Malvern, UK). The chemical structure of the PLGA-b-PEG copolymer was also analyzed by ^{1}H nuclear magnetic resonance (^{1}H NMR) (Bruker, AV400 NMR, USA) with $CDCl_3$ as a solvent and an attenuated total reflection Fourier transform infrared spectroscopy (ATR-FTIR) (Nicolet iS10, Thermo Scientific, USA) in the range of 500–4000 cm^{-1}.

2.5. Synthesis of curcumin-loaded magnetic polymeric nanoparticles

Curcumin-loaded magnetic polymeric nanoparticles (Cur-m-PNPs) were synthesized using the single emulsion solvent evaporation method with some modifications [43]. In brief, 20 mg PLGA-b-PEG di-block copolymer and 8 mg curcumin were co-dissolved in 4 mL of DCM in a glass vial. Then, 2 mg SPIONs was added to the solution, and the mixture was sonicated to form the organic phase. This organic phase was added dropwise into 20 mL of PVA solution (1%, w/v) and stirred for 10 min at 15,000 rpm by using an ultra-turrax homogenizer (IKA-T25, Germany). The emulsified solution was then stirred at 500 rpm for another 4 h to allow organic solvent evaporation. The reaction product, Cur-m-PNPs, was collected after centrifugation at 11,000 rpm (4 °C, 30 min) and subsequently washed with ultrapure water three times to remove all excess impurities and unloaded curcumin. Finally, nanoparticles were freeze-dried and kept at 4 °C for further use. For the synthesis of magnetic polymeric nanoparticles (m-PNPs), the method described above was utilized in the absence of curcumin in the organic phase.

2.6. Conjugation of GRGDS peptide to Cur-m-PNPs

Glycine-arginine-glycine-aspartic acid-serine (GRGDS) and carboxytetramethyl rhodamine (TAMRA)-labeled GRGDS (TAMRA-GRGDS) peptides were synthesized using standard Fluorenylmethyloxycarbonyl (Fmoc) chemistry by GeneCust (Luxemburg). The GRGDS and TAMRA-GRGDS peptides were purified by reverse-phase HPLC and verified using mass spectrometry. The conjugation of peptides with Cur-m-PNPs was performed *via* EDC-NHS reactions [42]. Briefly, 15 mg Cur-m-PNPs was homogeneously dispersed in 750 μL ultrapure water and then, 750 μL EDC-NHS was added to the NPs solution (75 mg EDC and 75 mg NHS 0.1 M MES (2-(N-morpholino)ethanesulfonic acid) buffer, pH: 5). The terminal carboxyl group of NPs was activated in a shaking incubator at 100 rpm for 45 min at 37 °C. The activated NPs were collected after centrifugation at 14,000 rpm (0 °C, 10 min) and washed with 0.1 M MES buffer once to remove all excess EDC-NHS. Thereafter, 750 μL of GRGDS or TAMRA-GRGDS (1 mg/mL, in MES buffer) peptide was added to the activated nanoparticles and allowed to slowly react for peptide conjugation at 37 °C and 100 rpm for 45 min. At the end of the reaction, the nanoparticles were washed two times with 0.1 M MES buffer for 10 min at 14,000 rpm and unbound peptides were removed.

The TAMRA-GRGDS peptide sequence was used to determine the amount of peptide that conjugated to m-PNPs or Cur-m-PNPs. TAMRA-GRGDS peptide, which contains fluorescent chemical groups, was conjugated to the surface of the NPs as described above. After the conjugation process, the washing solutions were collected in Falcon tubes and the peptide binding amount was determined using a fluorescence spectrophotometer (Cary Eclipse, Agilent, USA). For this purpose, TAMRA-GRGDS solutions were prepared in the range of 0–20 μg/mL and the calibration curve was obtained at 544 nm excitation and 572 nm emission wavelengths. All calculations were performed using the calibration curve. Also, TAMRA-GRGDS linked NPs were observed by fluorescence microscopy (Olympus IX71, Japan).

2.7. Characterization of nanoparticles

Morphology, size and size distribution of the obtained nanoparticles were examined by using transmission electron microscopy (TEM, FEI Tecnai G^2 Spirit BioTwin, USA) and scanning electron microscopy (Quanta 400F Field Emission SEM, USA). The average size and size distribution of NPs were calculated from TEM/SEM images using ImageJ software (National Institute of Health, USA).

The crystal structure of the superparamagnetic iron oxide nanoparticles (SPIONs) was investigated by X-ray diffraction (XRD) analysis (Rigaku, D/Max-B, Tokyo, Japan) using CuKα radiation at a scanning rate of 0.2°/min, from 20° to 80°. The average crystallite size of the SPIONs was also calculated based on the XRD pattern according to Scherrer's Eq. (1) [44]:

$$d = 0.9\lambda/\beta\cos\theta \quad (1)$$

Where d is the crystallite size, λ is the X-ray wavelength ($\lambda = 1.5405$ Å), β is the full width at half maximum (FWHM) and θ is Bragg's diffraction angle. The hydrodynamic size and size distribution of the nanoparticles were determined by dynamic light scattering (DLS) experiments using a Zetasizer Nano ZS (Malvern Instruments, UK) at room temperature. The presence of various functional groups on the surface of NPs was analyzed by ATR-FTIR spectroscopy in the range of 500–4000 cm^{-1} (Nicolet iS10, Thermo Scientific, USA). The magnetic field dependent magnetization of the SPIONs, PNPs, m-PNPs and Cur-m-PNPs were measured with quantum design physical property measurement system (QD-PPMS, USA) at room temperature in the field range between − 2 Tesla and + 2 Tesla. The heating potential of the magnetic nanoparticles (MNPs) was represented by the specific absorption rate (SAR) or specific loss power (SLP), which is defined as the heating power generated per unit mass. The magnitude of the SAR was calculated by Eq. (2) [45]:

$$SAR(W/g) = C\frac{m_{sol}}{m_{SPION}}\left(\Delta T \Big/ \Delta t\right) \quad (2)$$

Where the C is specific heat capacity for water ($C = 4.18$ J/g.°C), m_{sol} is the mass of entire solution, m_{SPION} is the mass of iron oxide nanoparticles, and $\Delta T/\Delta t$ is the initial slope of the time-dependent temperature curve. The temperature of the samples exposed to AC magnetic field was monitored by an infrared thermal camera (FLIR E6, Sweden). The iron content in each nanoparticle sample was quantified using a colorimetric method *via* an iron assay kit (Sigma Aldrich, MAK025) according to the manufacturer's instructions. The absorbance of the solutions was measured in 96 well plates using a microplate reader (Asys UVM 340, Austria) at 593 nm. Iron concentration of samples was calculated using a standard calibration curve. Standard solutions of known iron concentration were prepared also using iron assay kit components, and concentration range from 0 to 10 nmol/well (for 96 well plate).

2.8. Curcumin encapsulation efficiency and drug loading

Encapsulation efficiency (EE%) and drug loading capacity (DL%) of curcumin in Cur-m-PNPs and GRGDS-Cur-m-PNPs were determined by UV spectrometry (Nanodrop 2000c, Thermo scientific, USA). Briefly, lyophilized NPs were dissolved in acetonitrile (1 mg/mL) using an ultrasonic water bath and a magnetic stirrer. SPIONs and impurities were removed using neodymium magnet (magnetic separation) and centrifugation, respectively. The absorbance at 420 nm was measured in 4-fold diluted samples and the concentration of Cur was calculated using a standard curve of Cur constructed in acetonitrile (0–100 μg/mL). The EE% and DL% of NPs were calculated using Eq. (3) and Eq. (4):

$$EE\% = (\text{amount of Cur encapsulated in NPs/initially added amount of Cur}) \times 100 \quad (3)$$

$$DL\% = (\text{amount of Cur encapsulated in NPs/weight of NPs after lyophilization}) \times 100 \quad (4)$$

2.9. In vitro curcumin release

In vitro release of curcumin from Cur-m-PNPs and GRGDS-Cur-m-PNPs was carried out in phosphate buffer saline (PBS, pH: 7.4). The freeze-dried NPs were dispersed in PBS (2 mg/mL) and the solution was divided into microcentrifuge tubes (1000 μL each). The samples were incubated at 37 °C in a horizontal shaker at a speed of 100 rpm. After that, 2 μL of release medium was withdrawn at certain time intervals (0.5, 1, 2, 3, 6, 12, 24, 48, 72 h) and replaced with fresh medium. The released curcumin was dissolved in an equal volume of ethanol (2 μL) and the absorbance of the samples was measured by UV spectrophotometer at 430 nm. The *in vitro* Cur release from NPs was calculated using the standard curve of Cur constructed in ethanol/PBS (50:50, v/v) solutions at different concentrations (0–100 μg/mL). All the experiments were carried out in triplicate for each time point.

To realize the drug release mechanism of curcumin loaded m-PNPs, the experimental release data were fitted to the zero-order, first-order, Higuchi and Korsmeyer-Peppas kinetic models. The model equations are described below [46]:

$$\text{Zero-order kinetic model: } M_t/M_\infty = k_0 t \quad (5)$$

$$\text{First-order kinetic model: } \log(100 - W) = \log 100 - k_1 t \quad (6)$$

$$\text{Higuchi model: } M_t/M_\infty = k_H t^{1/2} \quad (7)$$

$$\text{Korsmeyer-Peppas model: } M_t/M_\infty = kt^n \quad (8)$$

where M_t/M_∞ is the fraction of the drug released at time *t*, *W* is the

drug release percentage at time t, t is the release time, k_0, k_1, k_H and k are kinetic rate constants of the zero-order, first-order, Higuchi, Korsmeyer-Peppas models and n is the release exponent indicative of the release mechanism of the drug.

2.10. Cell culture studies

Human glioblastoma cells (T98G cell line) were cultured in Dulbecco's Modified Eagle Medium F-12 with L-glutamine (DMEM F-12) supplemented with 10% (volume/volume, v/v) fetal bovine serum (FBS) and 1% (v/v) penicillin-streptomycin. Incubation processes were carried out at 37 °C in a humidified atmosphere containing 5% CO_2 (Heraeus Instruments, Germany).

2.10.1. Effects of free curcumin on T98G cells

T98G cells were seeded at a density of 10^4 cells/well in 96-well plates and incubated overnight. Curcumin was dissolved in dimethyl sulfoxide (DMSO) to prepare a stock solution of 10 mM. This solution was filtered through a 0.22 μm membrane and serial dilutions of Cur were prepared by using a culture medium. The cells were treated with medium containing an equivalent amount of DMSO (1%, v/v). As an additional DMSO-control group, cells were treated with DMSO (1%, v/v) alone in the medium. Subsequently, cells were treated with various concentrations of Cur (0–100 μM) for 24, 48, 72 h, and the cytotoxic effects were detected by 3-(4,5-dimethylthiazol-2-yl)-2,5-diphenyltetrazolium bromide (MTT) assay [47].

2.10.2. Effects of Cur-loaded m-PNPs on T98G cells

In the cell culture studies, magnetic polymeric nanoparticles (m-PNPs), GRGDS-conjugated magnetic polymeric nanoparticles (GRGDS-m-PNPs), curcumin-loaded magnetic polymeric nanoparticles (Cur-m-PNPs), and GRGDS-conjugated curcumin-loaded magnetic polymeric nanoparticles (GRGDS-Cur-m-PNPs) were used. T98G cells were seeded in a 96-well plate at a density of 10^4 cells/well and incubated at 37 °C in a humidified condition with 5% CO_2 overnight. Nanoparticles were sterilized by ultraviolet (UV) light for 10 min and dispersed in the culture medium. Then, the medium was replaced with the fresh one containing different concentrations (0–1000 μg/mL) of NPs. Also, cells were treated with an equivalent volume of NPs-free medium as a control group. The effect of nanoparticles on the proliferation of T98G cell lines was investigated at the 24th, 48th and 72nd h using the MTT assay and the 72nd h for live/dead cell viability assay. Furthermore, apoptotic/necrotic effect of NPs on T98G cells was analyzed after 72 h using the Annexin V-PI assay.

2.10.3. Hyperthermia treatments in vitro

In order to examine the effect of RF-hyperthermia on T98G cells, two types of experimental groups were established: only nanoparticles treated groups (NPs) and RF treated group (NPs+RF). The NPs+RF group was exposed to RF-field (13.56 MHz, 150 W, 15 min) in the presence of the NPs. T98G cells were seeded at a density of 2.5×10^5 cells per 25 cm^2 flask and incubated overnight to allow cell attachment. After incubation, the medium was replaced with a fresh medium, which contained 750 μg/mL of m-PNPs, Cur-m-PNPs or GRGDS-Cur-m-PNPs. Then, the cells were incubated for 24 h. Thereafter, the flasks were placed at the center of the solenoid coil and exposed to RF-hyperthermia for 15 min. During the exposure of hyperthermia, temperature elevation of the medium was monitored and measured by a thermal camera (FLIR E6, Sweden). Then, the cells were transferred to 96-well plate by trypsinization and incubated again for 24 h. Finally, MTT, live/dead and Annexin V-FITC/PI analyzes were performed.

2.10.4. MTT assay

After completion of the incubation time of free Cur, NPs or NPs+RF treatments on cells, 20 μL MTT solution (5 mg/mL) and 200 μL fresh medium were added to each well. After incubating for 3 h at 37 °C, the medium was aspirated, and replaced with 200 μL/well isopropanol. Cell viability was determined by measuring the absorbance of each well at 570 nm with a reference wavelength of 650 nm using a microplate reader (Asys UVM 340, Austria). Each experiment was repeated five times (n = 5). The concentration of free Cur or NPs that inhibited 50% cell growth compared with untreated cells (IC_{50}) was defined by curve fitting using GraphPad Prism software.

2.10.5. Live/dead cell viability analysis

The live/dead cell viability assay kit (K502-Biovision, USA) was used for the simultaneous determination of live and dead cells according to the manufacturer's instructions. The medium containing NPs was removed and 200 μL of assay buffer, 0.4 μL of live cell staining dye, and 0.2 μL of dead cell staining dye were added to each well, and cells were incubated for 15 min at 37 ℃ in the dark. Finally, stained live and dead cells were visualized by fluorescence microscopy (Olympus IX71, Japan).

2.10.6. Annexin V/PI double staining assay

Apoptotic cells were monitored by Annexin V-FITC/PI staining using an apoptosis detection kit (K101-Biovision, USA) according to the manufacturer's instructions. The medium containing NPs was removed and 100 μL of 1X binding buffer, 1 μL of Annexin V-FITC and 1 μL of propidium iodide were added to each well and incubated in the dark for 5 min at room temperature, thereafter early apoptotic, late apoptotic or necrotic cells were detected by using fluorescence microscopy (Olympus IX71, Japan).

2.10.7. Cellular uptake

Fluorescent dye labeled-peptide (TAMRA-GRGDS) conjugated to NPs surface was enabled to tracking the NPs in T98G cells. Briefly, T98G cells were seeded in a 24-well plate and then, incubated overnight. After incubation, TAMRA-GRGDS conjugated Cur-m-PNPs (250 μg/mL) were added to certain wells. After 2 h and 24 h of incubation time, cells were washed twice with PBS and observed using fluorescence microscopy. Cellular uptake of the nanoparticles was also quantitatively analyzed by calculation of Pearson's correlation coefficient (PCC) and Manders' colocalization coefficients (MCC) using JACoP in ImageJ v1.53 software (National Institute of Health, USA). The Pearson coefficient indicates how well green (Cur) and red (TAMRA) fluorescent intensities are correlated for every pixel of an images whereas Manders' M1 and M2 coefficients are the indicators of the fraction of red fluorescence overlapping green and vice versa, respectively [48]. Values close to 1 indicates better colocalization of the green and red fluorescence for both coefficients.

2.11. Statistical analysis

Results were presented as mean ± standard deviation (SD) of five times replicated measurements in a parallel manner unless otherwise indicated. Statistical significance of difference was tested either students' t-test or one-way analysis of variance (ANOVA) test with Dunnett's post-test. The significance level was set at 0.05. All data that required non-linear regression analysis were performed using GraphPad Prism version 9 (GraphPad Software Inc., CA, USA). P value less than 0.05 was considered as statistically significant ($^*p < 0.05$, $^{**}p < 0.01$, $^{***}p < 0.001$).

3. Results and discussion

3.1. Synthesis and characterization of superparamagnetic iron oxide nanoparticles

Superparamagnetic iron oxide nanoparticles (SPIONs) were synthesized by thermal decomposition of organo-iron precursor in the presence of oleic acid (OA) in a high-boiling point organic solvent (1-octadecene)

[41]. TEM images revealed the highly monodisperse SPIONs (Fig. 1a) with a mean particle size of 5.6 ± 0.9 nm and the size distribution of SPIONs was quite narrow (Fig. 1b). The crystalline structure of SPIONs was determined by XRD (Fig. 1c). The characteristic peaks for Fe_3O_4 ($2\theta = 30.24°$, 35.6°, 43.26°, 53.7°, 57.11°, 62.82° and 74.23°) marked by their indices ((220), (311), (400), (422), (511), (440) and (533)), were observed for SPIONs. These peaks are consistent with the database in the JCPDS file (JCPDS card no. 01-075-0449) with a cubic structure [49]. Also, the size of crystallite was calculated by using Scherrer's equation as 8.32 nm. The adsorption of OA on the surface of Fe_3O_4 NPs was shown by ATR-FTIR spectroscopy (Fig. 1d). The pure OA shows two peaks at 2855 and 2920 cm^{-1} corresponding to the symmetric and asymmetric $-CH_2$ stretching, respectively. The intense peak at 1707 cm^{-1} attributed to $-C{=}O$ stretch and the peak at 1286 cm^{-1} corresponds to C–O stretch. In the ATR-FTIR spectrum of OA coated Fe_3O_4 NPs, the symmetric CH_2 stretch was shifted to a lower frequency (2851 cm^{-1}). The displacement to a lower frequency indicates that the OA layer adsorbed onto the surface of the NPs and hydrocarbon molecules surrounding the NPs were in a close-packed ordering [50]. The presence of magnetite is characterized by two bands at 634 and 590 cm^{-1}, which attributed to the Fe–O stretching [51]. Also, 1641 cm^{-1} and 1464 cm^{-1} peaks correspond to asymmetric and symmetric carboxylate vibrations, respectively, which indicate that the bonds between iron atoms and carboxylate groups of OA have been established [52]. Overall, these results confirm that the synthesis of the OA coated Fe_3O_4 NPs by thermal decomposition was successful.

3.2. Synthesis and characterization of m-PNPs and Cur-m-PNPs

To obtain magnetic polymeric nanoparticles (m-PNPs), PLGA-b-PEG di-block copolymer was first synthesized using PLGA and PEG polymers *via* EDC-NHS chemistry. The successful conjugation of PLGA and PEG polymers was confirmed by analyzing the characteristic peaks of the synthesized PLGA-b-PEG, using both ^1H NMR and ATR-FTIR spectra. The ^1H NMR spectrum of the PLGA-b-PEG showed both characteristic peaks of PLGA and PEG (Fig. S2a). The peaks at 1.6 ppm ($-CH_3$), 4.8 ppm ($-CH_2$) and 5.2 ppm (–CH) represent PLGA structure [53], while the peak at 3.4 ppm ($-CH_2CH_2O-$) denotes the presence of the PEG structure in the synthesized PLGA-b-PEG [54]. Also, the molecular weight of PLGA-b-PEG was determined by GPC, yielding M_n:14.4 kDa, M_w:31.5 kDa and polydispersity index = 2.18. The synthesis yield of PLGA-b-PEG was 80%, and PEGylation efficiency was 50% in terms of 0.5% w/w PEG in the synthesized PLGA-b-PEG. According to ATR-FTIR analysis (Fig. S2b), an intense peak at 1746 cm^{-1} corresponds to the $C{=}O$ stretching of PLGA was observed in the synthesized copolymer. The presence of PEG can be noticed by the small peaks at 950 cm^{-1} and 841 cm^{-1}, which represent C–H bending vibration and C–O–C stretching, respectively. Moreover, the peak at 1673 cm^{-1} represents the hydrogen-bonded carbonyl of the amide, indicating that a carbonyl amide linkage (CO-NH) was successfully generated [53,54]. Overall, the synthesis of the PLGA-b-PEG copolymer was successfully carried out based on both ^1H NMR and FTIR results. After this section, PLGA-b-PEG di-block copolymer has been abbreviated simply as polymer. For example, PLGA-b-PEG nanoparticles have been abbreviated as polymeric nanoparticles (PNPs).

Morphology and size of magnetic polymeric nanoparticles (m-PNPs) were determined using TEM, SEM and DLS analyses (Fig. 2a–d). According to SEM analysis, the m-PNPs exhibited spherical morphology with a mean diameter of 167 ± 64 nm (Fig. 2a and c). TEM confirmed that encapsulation of SPIONs has been clearly illustrated with uniform magnetic nanoparticle distribution (black spots in Fig. 2b) within the polymeric matrix. Moreover, the image showed that SPIONs exhibited well-defined spherical shape in the core and no apparent particle aggregation was observed in polymeric nanoparticles. The dynamic light scattering (DLS) measurements also revealed that the average hydrodynamic diameter of m-PNPs is 247 ± 90 nm (Fig. 2d). The different particle sizes obtained by SEM and DLS are due to the difference between the operating conditions of these methods. DLS measures a hydrodynamic diameter of NPs in an aqueous solution; therefore, NPs are in a swollen state, while SEM/TEM analyses of NPs have been performed after drying process [50]. Also, the interaction of multiple parameters in DLS, including the concentration, shape, and surface properties of the NPs, can contribute to the size difference obtained from DLS [55].

In Fig. 2e, the SEM image of the curcumin-loaded magnetic polymeric nanoparticles (Cur-m-PNPs) showed a spherical shape, and the diameter was about 142 ± 70 nm (Fig. 2f). In addition, the DLS results showed that the average hydrodynamic diameter of Cur-m-PNPs was 215 ± 70 nm (Fig. 2g). Consequently, the NPs with regular size and shape were successfully produced and characterized.

The magnetic field-dependent magnetizations of the NPs were shown in Fig. 2h. It is clear to find that magnetization curves of all the samples exhibit superparamagnetic behavior, in which the coercivity are close to zero. The magnetization (M_s) of the PNPs was found to be zero (no iron content) as expected. The saturation magnetization of the SPIONs were found as 6.0 emu/g and this value is relatively low compared to the literature findings [56]. However, magnetic properties of SPIONs strongly affected by their size. Smolensky et al. have found that the M_s values of the SPIONs decreased from 43 emu/g to ~3 emu/g as the particle size changing from 18 to 5 nm [57]. This could be attributed to the distortion of the crystal symmetries 'spin canting effect' of the magnetic dipole moments as the particle size decreases [58]. As expected, M_s of the m-PNPs and Cur-m-PNPs decreased to 0.6 and 0.3 emu/g, respectively. The decrease in M_s values of the polymeric nanoparticles is mainly due to the dense PLGA layers around SPIONs for m-PNPs, and additionally curcumin content for Cur-m-PNPs. By using the ΔT *vs.* t graph (Fig. S7), SAR values were calculated as 315 W/g for m-PNPs, 310 W/g for Cur-m-PNPs and 330 W/g for GRGDS-Cur-m-PNPs. These SAR values are consistent with Nehate et al. [59]. Overall, the findings in this study confirm the capability of these nanoparticle systems that can generate heat to increase the temperature of the cell culture medium to the hyperthermia treatment degrees (~42–45 °C) during 15 min of AC magnetic field exposure.

ATR-FTIR analysis of Cur, m-PNPs and Cur-m-PNPs was shown in Fig. 2i. In the free Cur spectrum, 3503 cm^{-1} corresponds to O–H stretching. 1626 $cm^{-1}$and 1601 cm^{-1} attributed to $C{=}O$ vibration and $C{=}C$ aromatic stretch, respectively, and both peaks were also seen in Cur-m-PNPs. In addition, 1750 cm^{-1} and 2946 cm^{-1} peaks correspond to the $C{=}O$ stretch and aliphatic CH band of the PLGA polymer [60], these peaks were observed on both m-PNPs and Cur-m-PNPs. Our results are consistent with the related literature [61]. Cur-loaded m-PNPs with suitable size that can be used in the treatment of GBM have been successfully produced.

Following NPs fabrication and detailed characterization studies, TAMRA labeled GRGDS was chemically immobilized on m-PNPs and Cur-m-PNPs with EDC-NHS chemistry. Mass spectroscopy analysis revealed that GRGDS and TAMRA-GRGDS peptides had molecular weights of 490.47 and 1031.09 g/mol ($[M-H]^-$), respectively, which matches the theoretical molecular weights of peptides (Fig. S3a,b). According to HPLC analysis, GRGDS and TAMRA-GRGDS peptides have ~99% and ~95% purity (Fig. S4a,b), respectively, and they can be used for *in vitro* studies without further purification. The conjugation amount of GRGDS onto the m-PNPs and Cur-m-PNPs were found as ~37 μg peptide/mg NP for both NPs, according to the absorbance-concentration standard curve of TAMRA-GRGDS (Fig. S5). It was confirmed that GRGDS peptide had been successfully conjugated onto m-PNPs and Cur-m-PNPs, which would ensure the targeting ability for subsequent experiments.

3.3. Loading and release studies of curcumin

The encapsulation efficiency and drug loading of Cur-m-PNPs were calculated to be 25% and 8%, respectively. After conjugation of GRGDS

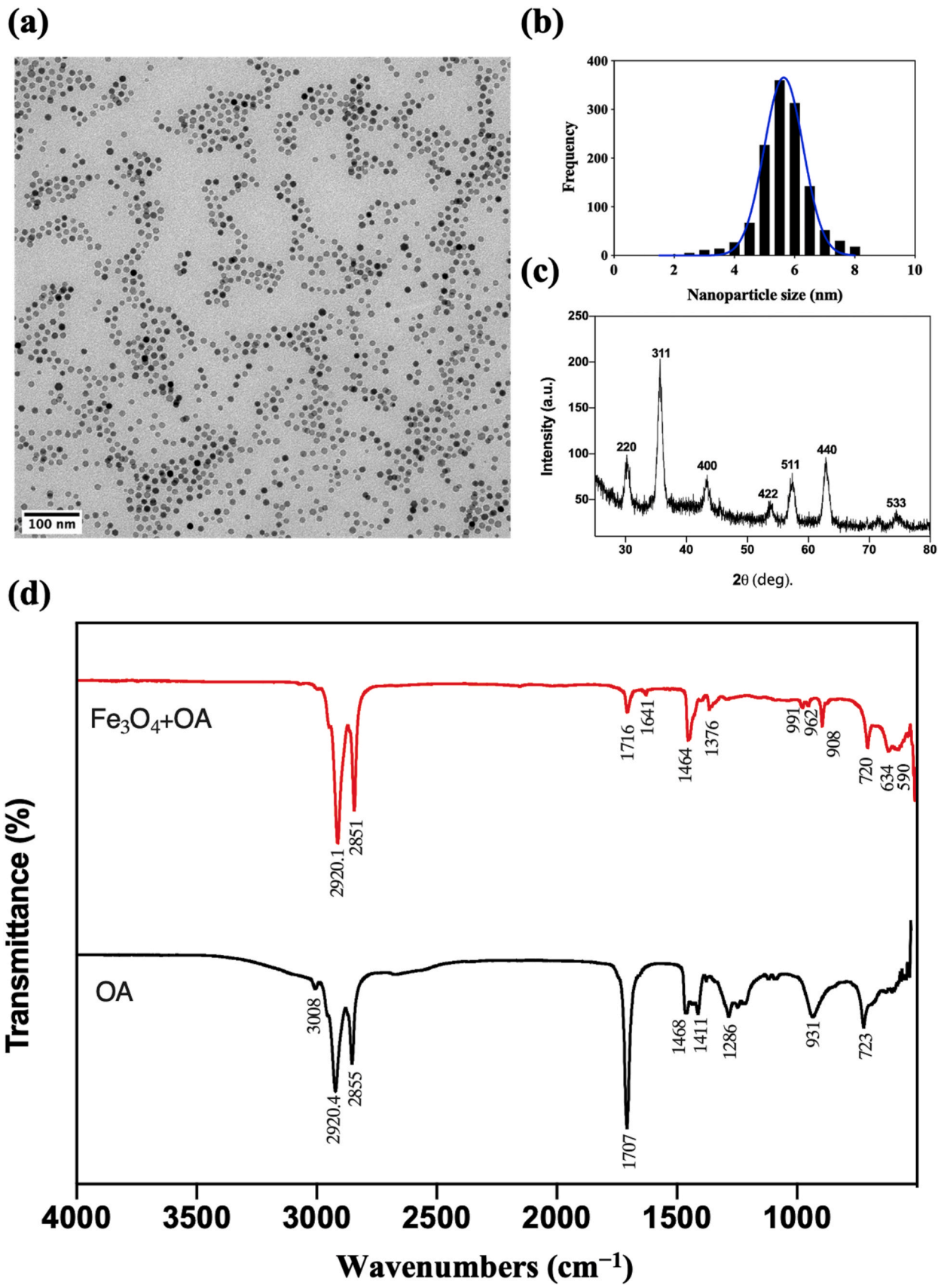

Fig. 1. (a) TEM image, (b) size distribution histogram, (c) XRD pattern of SPIONs (Fe_3O_4 + OA) and (d) ATR-FTIR spectra of oleic acid (OA) and SPIONs.

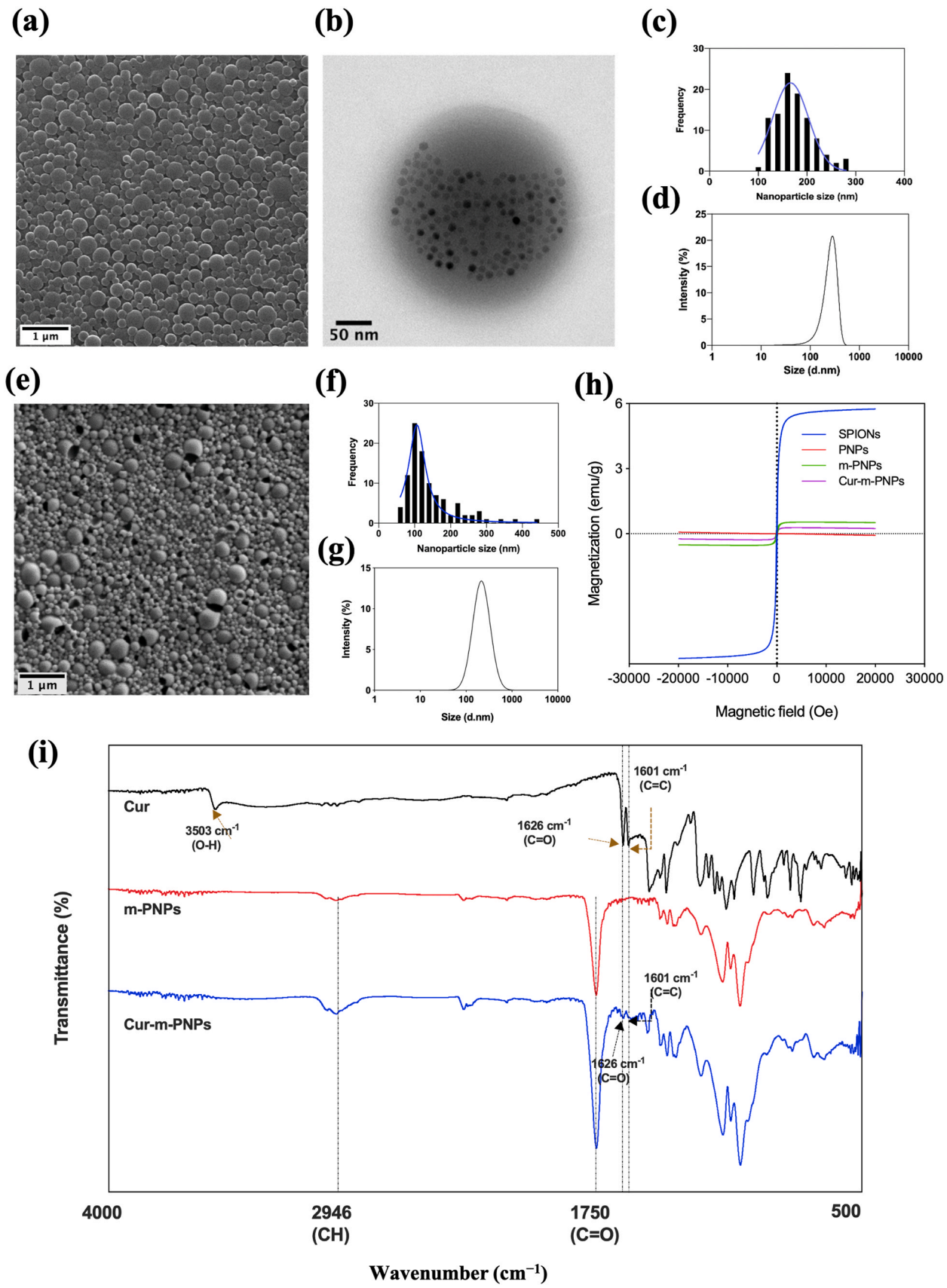

Fig. 2. Magnetic PNPs (a) SEM image, (b) TEM image, (c) size distribution histogram obtained from SEM image, (d) hydrodynamic size distribution; Cur-m-PNPs (e) SEM image, (f) size distribution histogram obtained from SEM image, (g) hydrodynamic size distribution, (h) magnetization *vs.* applied magnetic field curve for SPIONs, PNPs, m-PNPs and Cur-m-PNPs, (i) ATR-FTIR spectra of free Cur, m-PNPs and Cur-m-PNPs.

to Cur-m-PNPs, the EE% and DL% values of GRGDS-Cur-m-PNPs decreased to 4.0% and 1.6%, respectively. These reductions are probably due to the leaking of Cur from polymeric NPs during three times washing and shaking in the incubator for the peptide conjugation process. Jamali et al. reported that a decrease of EE% and DL% values of Cur-PLGA NPs (66%, 11%, respectively) after MAb-antibody conjugation to Cur-PLGA NPs (27%, 4.5%, respectively) [61]. Also, the EE% value of Cur in PLGA NPs were reported as 31% [62] and 22% [63] in previous studies, which was consistent with our results.

The *in vitro* Cur release profile from Cur-m-PNPs and GRGDS-Cur-m-PNPs in PBS (pH = 7.4, 37 °C) during 72 h was shown in Fig. 3. Curcumin release from Cur-m-PNPs and GRGDS-Cur-m-PNPs occurred in a biphasic manner, with an initial burst phase and then, a sustained-slower phase. Cur-m-PNPs showed 40% Cur release in the first 3 h followed by sustained release of 72% over the entire period of the study. Also, GRGDS-Cur-m-PNPs showed 31% and 65% of Cur release, at the 3rd h and the 72nd h, respectively. However, there was no significant difference between the release curves of Cur-m-PNPs and GRGDS-Cur-m-PNPs (Fig. 3).

As shown in Fig. 3, curcumin release from m-PNPs shows two distinct phases: a fast release phase between 0 and 3 h and a slow-release phase between 3 and 24 h and the release was almost completed after 24 h. This drug release profile can be explained as burst biphasic [64]. Therefore, the experimental release data was analyzed by a two-step approach between 0 and 3 h (Stage 1-fast period) and 3–24 h (Stage 2-sustained release period) to explore the mechanism of curcumin release from m-PNPs. The experimental release data were fitted to four kinetics models (Fig. 4) and the rate constants and the regression coefficient (R^2) values were calculated based on the fitted curves (Table 1). The R^2 closest to 1 indicates the best kinetic model the drug release mechanism obeys. The zero-order kinetic model indicates that the drug release rate from a reservoir is independent of its concentration (only time dependent). On the other hand, the first order kinetic model defines a concentration dependent release profile. Also, Higuchi model is mainly used to describe diffusion-controlled drug release based on Fick's law [65]. According to the R^2, the highest correlation for Cur-m-PNPs in Stage 1 (R^2 = 0.942) and Stage 2 (R^2= 0.991) was observed in the Higuchi model which means that the curcumin release in all stages from these nanoparticles was diffusion-controlled. Moreover, rate constant for Higuchi model (k_H) decreased from 0.248 $h^{-1/2}$ to 0.080 $h^{-1/2}$ confirming that the sustained release of curcumin started after 3 h of initial fast release period. After GRGDS conjugation, drug release mechanism was orchestrated by first-order kinetic with R^2 value of 0.983 for fast release period (0–3 h). This shows that the GRGDS conjugation to the Cur-m-PNPs surface may act as an extra diffusion barrier for curcumin to be released and the release system becomes concentration dependent. According to the drug release mechanism, we can say that surface adsorbed and loosely bound curcumin to the GRGDS conjugated Cur-m-PNPs was released to the sink in a concentration dependently manner during the fast release period. After an initial burst period, curcumin release from GRGDS-Cur-m-PNPs followed again a Fickian diffusion with an R^2 value of 0.969 for Higuchi model. To further analyze drug release mechanism from the m-PNPs, the experimental release data were also fitted to Korsmeyer-Peppas model [66]. Korsmeyer-Peppas equation is a useful mathematical model to identify the drug release mechanism when more than one type of release mechanism is involved. In this model, the n value characterizes the release mechanism of a drug. For spherical particles, a value of $n \leq 0.43$ corresponds to a Fickian diffusion mechanism whereas an n value between 0.43 and 0.85 states a non-Fickian or anomalous transport. If the n value is greater than 0.85, drug release mechanism is characterized as the Super Case II model. The Super Case II model is observed when the released solvent shows a high affinity to the drug carrier matrix. In the case of Cur-m-PNPs, the n value was found as 0.52 for Stage 1 and 0.24 for Stage 2 with the R^2 values of 0.856 and 0.992, respectively. Korsmeyer-Peppas kinetic parameters cannot be used to define the release mechanism for the Cur-m-PNPs at Stage 1 since the release data did not fit this model well enough due to a low R^2 value. However, Fickian diffusion mechanism can be used to explain curcumin release from Cur-m-PNPs by Higuchi model for Stage 1 (R^2 = 0.942) and both

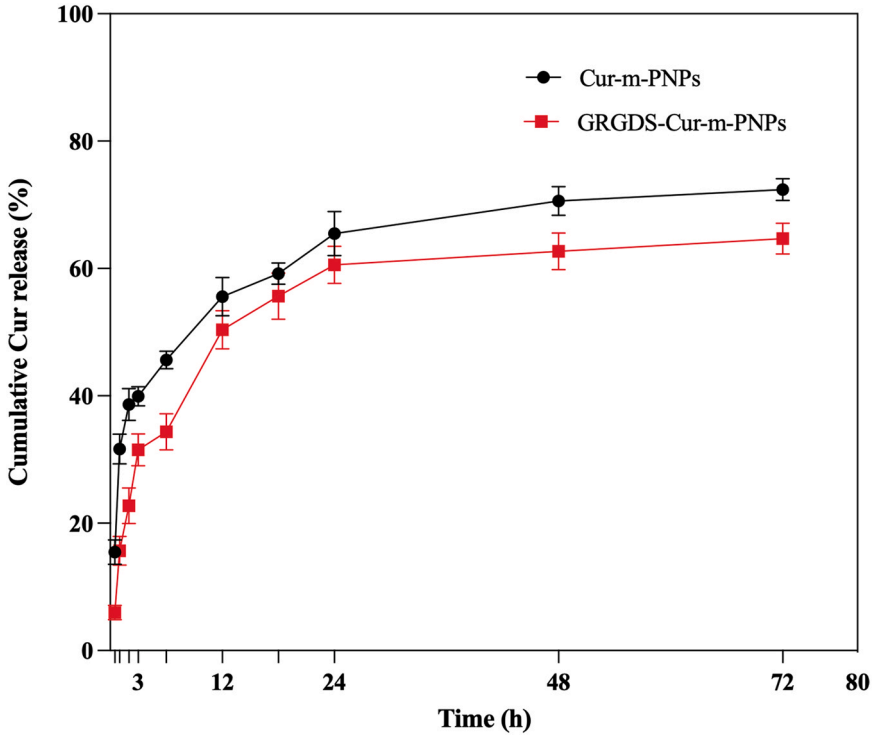

Fig. 3. *In vitro* release profile of curcumin from Cur-m-PNPs and GRGDS-Cur-m-PNPs in PBS (pH = 7.4) at 100 rpm in a shaking incubator (37 °C). All release assays were performed in triplicate and the mean ± SD are shown.

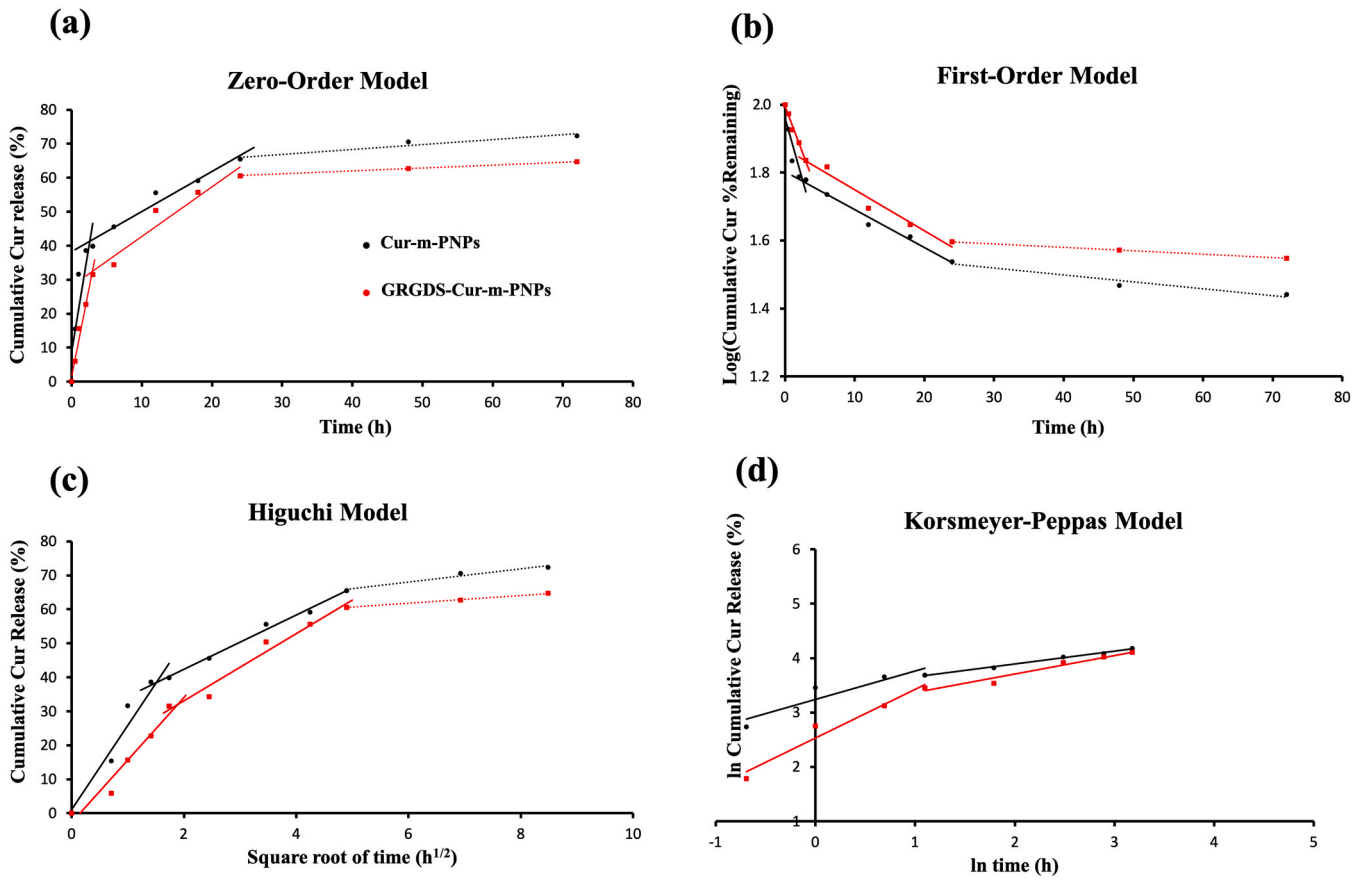

Fig. 4. Kinetic analysis plots of (a) zero-order, (b) first-order, (c) Higuchi and (d) Korsmeyer-Peppas models for curcumin release.

Table 1
The Cur release constants and correlation coefficients (R^2) obtained from various kinetic models for Cur-m-PNPs and GRGDS-Cur-m-PNPs.

		Zero-order		First-order		Higuchi		Korsmeyer-Peppas		
		k_0	R^2	k_1	R^2	k_H	R^2	k	n	R^2
Cur-m-PNPs	Stage 1	0.126	0.787	0.166	0.823	0.248	**0.942**	0.26	0.52	0.856
	Stage 2	0.012	0.965	0.026	0.983	0.080	**0.991**	0.30	**0.24**	**0.992**
GRGDS-Cur-m-PNPs	Stage 1	0.103	0.971	0.125	**0.983**	0.184	0.950	0.13	**0.89**	**0.955**
	Stage 2	0.015	0.943	0.028	0.966	0.099	**0.969**	0.21	**0.34**	**0.958**

Higuchi model ($R^2 = 0.991$) and Korsmeyer-Peppas model ($R^2 = 0.992$, $n = 0.24$) for Stage 2. On the other hand, the n value for the fast release period from GRGDS-Cur-mPNPs is calculated as 0.89 ($R^2 = 0.955$) indicating the non-Fickian Super Case II drug transport. This can be attributed to the GRGDS peptide cover on m-PNPs increased the water affinity of the polymeric matrix, thereby, drug release takes place by the

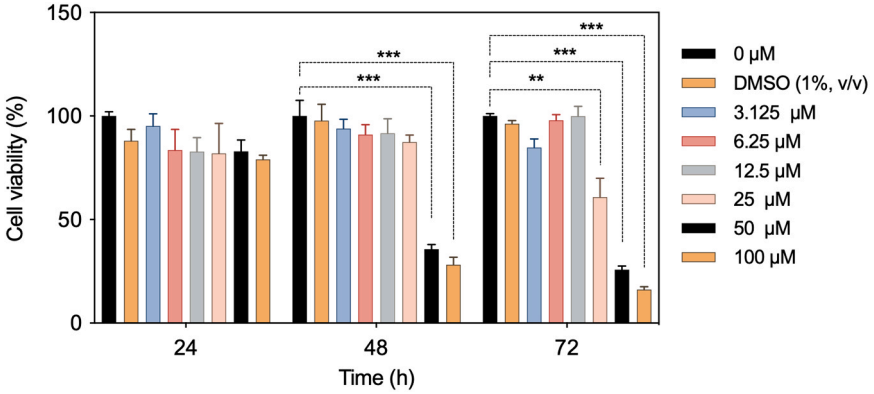

Fig. 5. *In vitro* cytotoxicity of free curcumin after 24 h, 48 h and 72 h treatment on T98G cell lines. Cell viability assay was performed by MTT assay. Values represent mean ± SD (n = 5), $*p \leq 0.05$, $**p \leq 0.01$, $***p \leq 0.001$.

combination of diffusion and polymer relaxation [67]. In Stage 2, curcumin release from GRGDS-Cur-m-PNPs follows a Fickian diffusion with an *n* value of 0.34.

3.4. Cytotoxicity of free curcumin against T98G cell lines

The cytotoxicity of free curcumin was investigated on T98G glioblastoma cells at different concentrations (0–100 μM) for 24, 48 and 72 h by MTT assay (Fig. 5). The free Cur exhibited dose-dependent cytotoxicity with increasing Cur concentration for 48 and 72 h on T98G cells. The DMSO-control group did not show any effect on cell growth for all incubation times. The IC_{50} values of Cur for T98G cell lines were reported as 8 μM [68] and 50 μM [69] after 24 h; 18 μM [70] after 120 h on the previous studies. In this study, the IC_{50} value of free Cur was found as 36 μM after 72 h, which could be used as a reference concentration for subsequent cell cytotoxicity of Cur-m-PNPs or GRGDS-Cur-m-PNPs.

3.5. Cytotoxicity of NPs against T98G cells

The therapeutic efficacy of m-PNPs, GRGDS-m-PNPs, Cur-m-PNPs and GRGDS-Cur-m-PNP was investigated on T98G cells for 24 h, 48 h

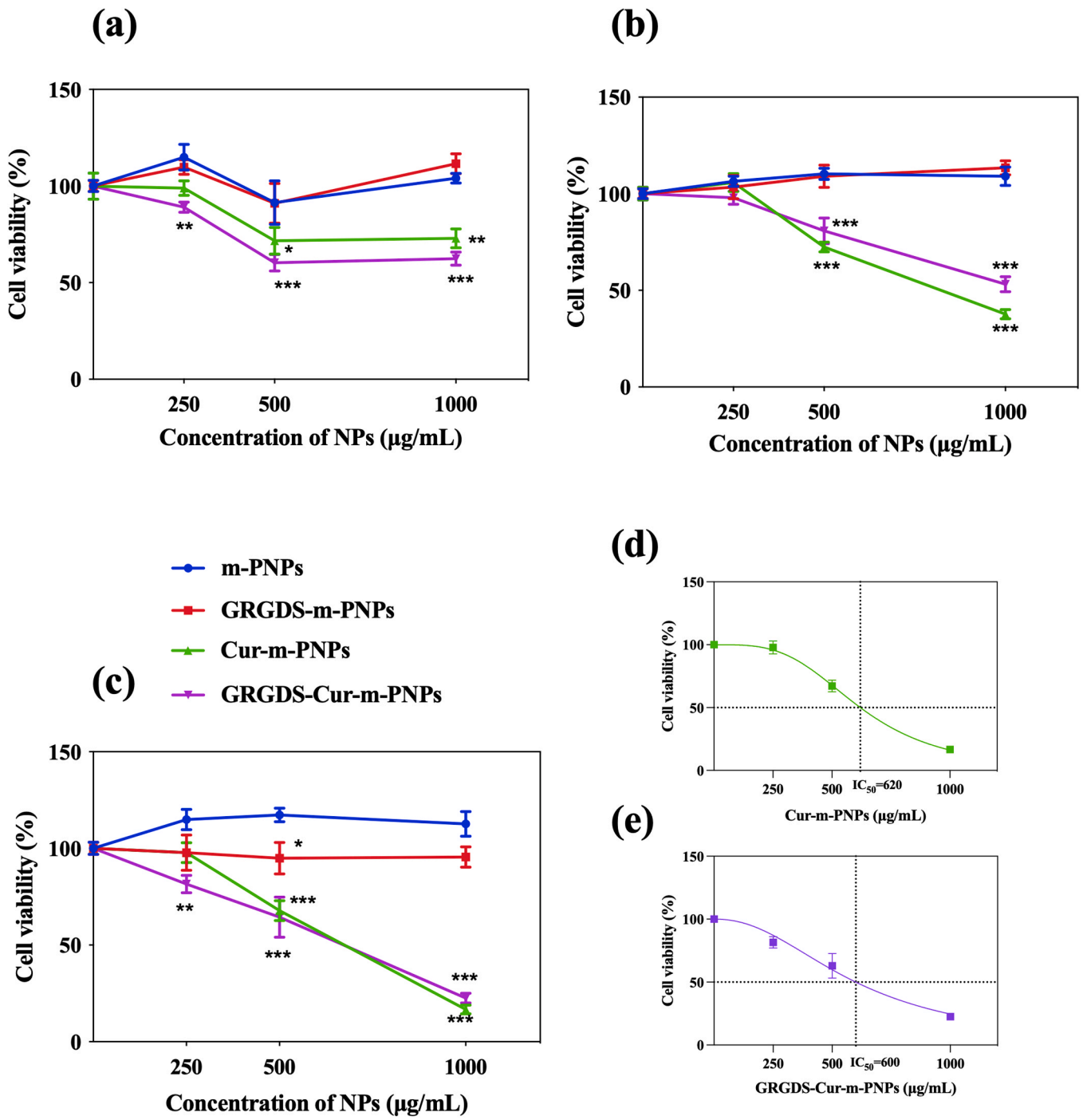

Fig. 6. *In vitro* cytotoxicity of nanoparticles after (a) 24 h, (b) 48 h and (c) 72 h treatments on T98G cell lines; the graphs representing the IC_{50} values of (d) Cur-m-PNPs and (e) GRGDS-Cur-m-PNPs. Cell viability assay was performed by MTT. The statistical comparison of differences among NPs at the same dose was analyzed. Values represent mean ± SD (n = 5), $*p \leq 0.05$, $**p \leq 0.01$, $***p \leq 0.001$.

and 72 h by MTT assay (Fig. 6). GRGDS-m-PNPs had no significant toxic effect on T98G cells compared to m-PNPs for all incubation times. This result confirmed that both m-PNPs and GRGDS-m-PNPs exhibited no cytotoxicity against T98G cells, suggesting good biocompatibility of the drug carriers and targeting peptides. However, both Cur-m-PNPs and GRGDS-Cur-m-PNPs caused a significant decrease in cell viability compared to m-PNPs for all incubation times (Fig. 6). The cytotoxic effects of the NPs on the T98G cells were determined by evaluating the IC_{50} values and these values were compared with free Cur (Table 2). The cytotoxicity of GRGDS-Cur-m-PNPs was found to be almost 2.5-fold higher than that of free Cur and 6-fold higher than that of Cur-m-PNPs for 72 h. Since curcumin was released from Cur-m-PNPs and GRGDS-Cur-m-PNPs in a sustained manner for up to 72 h, the therapeutic effects of NPs on T98G cells were evaluated especially for 72 h (Table 3).

The increase of potential therapeutic efficiency of GRGDS-Cur-m-PNPs was probably due to the success of enhanced cellular uptake and targeting ability of NPs. Also, results showed that GRGDS-Cur-m-PNPs inhibited the proliferation of T98G cells more effectively than that of free Cur and Cur-m-PNPs. Therefore, GRGDS-Cur-m-PNPs could enhance *in vitro* anticancer effectivity of Cur. Besides, the cytotoxic effect of Cur-loaded NPs on T98G cells was supported by live/dead cell staining (Fig. 7a). These fluorescence images were consistent with the results of MTT analysis. Jiang et al. showed that RGD-linked, paclitaxel and curcumin co-loaded liposomes showed a superior anti-proliferative effect on A549 cells (lung cancer cell lines) with synergistic therapeutic effect for targeted-chemotherapy [71].

Apoptosis is related to loss of membrane asymmetry causing the externalization of phosphatidylserine (PS) from the inner to the outer of the plasma membrane [72]. The use of propidium iodide (PI) and FITC-labeled Annexin V (Annexin V-FITC) is a typical technique to display the progression of apoptosis [73]. Early apoptotic cells were Annexin V-positive and PI-negative, whereas late apoptotic or necrotic cells were Annexin V/PI double-positive. Annexin V-FITC/PI staining was performed for the evaluation of apoptosis/necrosis after the treatment of Cur-m-PNPs and GRGDS-Cur-m-PNPs on T98G cells, and cells were observed using fluorescence microscopy (Fig. 7b). In general, the cells treated with GRGDS-Cur-m-PNPs underwent a higher level of early apoptotic cells as compared to those treated with Cur-m-PNPs. T98G cells treated with Cur-m-PNPs showed intensively stained nucleus that the membrane integrity was completely disrupted. Wadajkar et al. developed a magnetic-based core-shell particle conjugated with GRGDS peptide for targeting melanoma cells, and they found that the cellular uptake of GRGDS-conjugated particles was higher than that of the non-conjugated particles by melanoma cells [74]. In another study, RGE-conjugated and SPION-Cur co-loaded exosomes showed the highest targeting ability depending on the presence of RGE peptide on U251 cells [3]. Quader et al. showed that epirubicin (potential anti-GBM agent) loaded polymeric micelles with cyclic-RGD conjugation were uptaken by GBM cells faster and in a higher amount than those without RGD [4]. In our study, the GRGDS peptide has been successfully used as a targeting agent for T98G cells, and GRGDS-conjugated NPs were found to reduce the effective dose of curcumin 6-fold compared to those without GRGDS.

3.6. Cellular uptake

To further investigate the correlation between the enhanced cytotoxic effect of the GRGDS-targeted NPs and cellular uptake by the T98G cells, TAMRA-labeled GRGDS-Cur-m-PNPs were tracked in T98G cells using fluorescence microscopy (Fig. 8). As shown in Fig. 7, the green signal of curcumin and red signal of TAMRA appear in the T98G cells after 2 h and 24 h incubation with 250 μg/mL TAMRA-GRGDS-Cur-m-PNPs (containing 4 μg/mL Cur). In Fig. 8, when the images were overlapped, the green and red fluorescent were approximately co-localized (yellow), and this also indicated that GRGDS-peptide was successfully conjugated to the surface of NPs. In addition, Fig. 8 (merged) exhibited that NPs entered into the cells after incubation for 2 h and the co-localized (TAMRA-Cur) fluorescent colors enable to track the location of the NPs. After 24 h incubation time, T98G cells became shrunken, rounded, and most of the NPs accumulated inside the cells. The colocalization studies can be displayed in scatterplots where the intensity of red color is plotted against the intensity of green color for each pixel, just like the output presented as flow cytometry data [48]. Pearson's correlation coefficient (PCC) and Mander's M1 and M2 coefficients were calculated as 0.89, 0.97 and 0.82 after 2 h of incubation, respectively and these values changed to 0.98, 0.92 and 0.99 for 24 h (Fig. 8). At the longer incubation period (24 h), the green and red fluorescence intensities overlapped perfectly in both coefficients. In summary, qualitative and quantitative analyses of the fluorescence images indicated that GRGDS-Cur-m-PNPs was efficiently delivered into the cells, and most probably GRGDS contributed to the enhanced therapeutic efficiency of NPs.

3.7. In vitro hyperthermia application

We have previously shown that the presence of GRGDS on NPs improved the cytotoxicity of Cur-m-PNPs 6-fold by decreasing the effective dose of curcumin (Fig. 6). To evaluate the combined effect of hyperthermia with targeting, glioblastoma cells were exposed to RF-hyperthermia in the presence of m-PNPs, Cur-m-PNPs or GRGDS-Cur-m-PNPs. The treatment concentration of Cur-m-PNPs and GRGDS-Cur-m-PNPs incubated with the cells was determined as 750 μg/mL for hyperthermia. Cur concentrations in 750 μg NPs were calculated by considering the loading and releasing amounts of Cur for 24 h, as shown in Table 4. These values were approximately compatible with the IC_{50} values of NPs (according to the amount of Cur) which was previously

Table 2
IC_{50} values of free Cur, Cur-m-PNPs and GRGDS-Cur-m-PNPs on T98G cells after 72 h.

T98G	Free Cur	Cur-m-PNPs (amount of Cur loaded and released)	GRGDS-Cur-m-PNPs (amount of Cur loaded and released)
IC_{50} (72 h)	36 μM	~620 μg/mL (~90 μM Cur)	~600 μg/mL (~15 μM Cur)

Table 3
Concentrations of Cur-m-PNPs and GRGDS-Cur-m-PNPs decided for the treatment of T98G cells in the view of the loading and 72 h releasing amounts of Cur.

Parameters	Cur-m-PNPs	GRGDS-Cur-m-PNPs
Drug loading (DL%, w/w)	8	1.6
μM Cur/mg NPs	~200 μM	~40 μM
Cur release from NPs in 72 h	72	65
μM Cur/mg NPs (release in 72 h)	144 μM	26 μM
The doses of NPs treated to T98G	250; 500; 1000 μg/mL	250; 500; 1000 μg/mL
The doses of NPs treated to T98G (by the amount of Cur loading and releasing for 72 h)	36; 72; 144 μM, respectively	6.5; 13; 26 μM, respectively

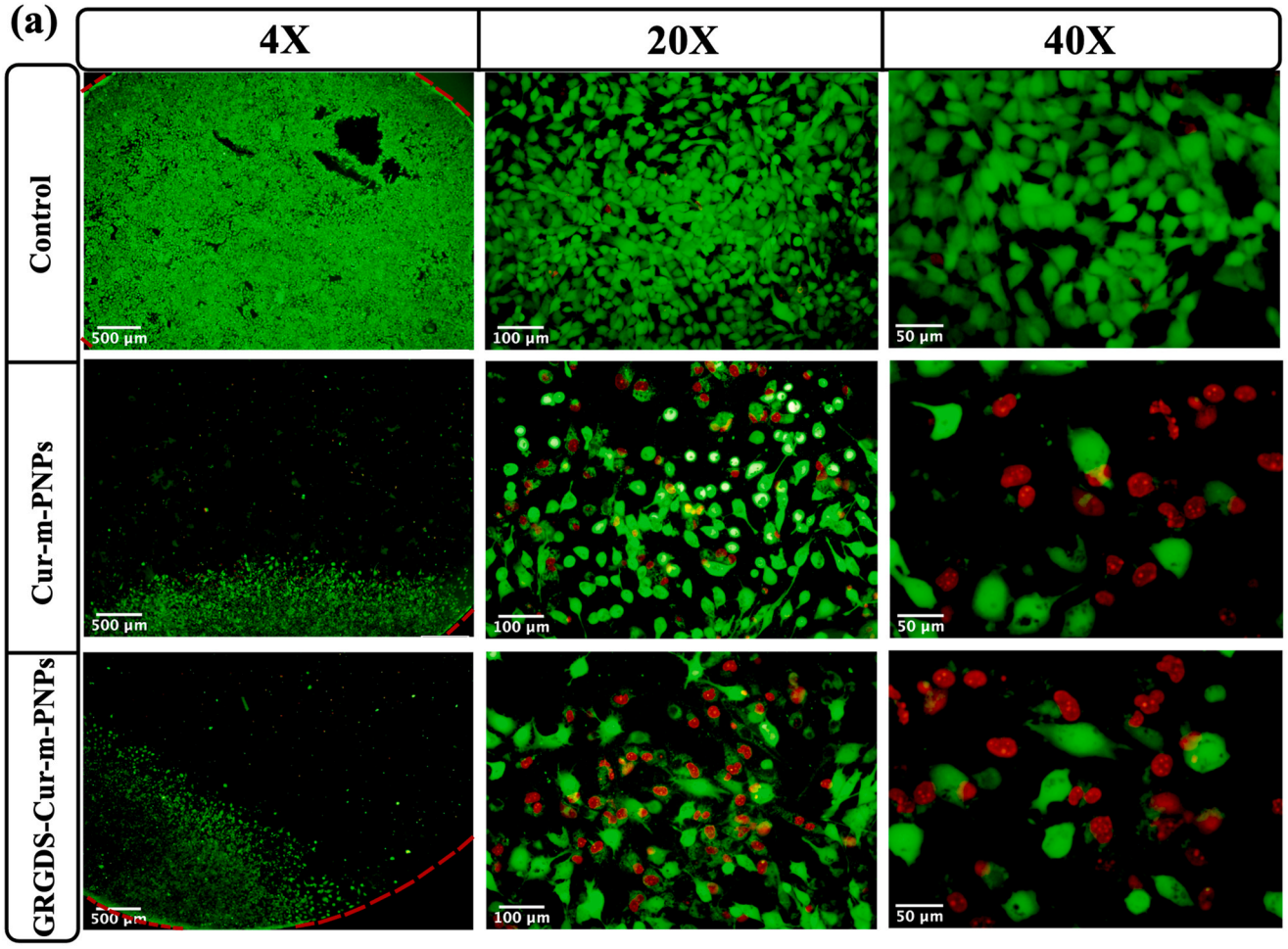

Fig. 7. (a) The fluorescence images of T98G cells after 72 h incubation with Cur-m-PNPs or GRGDS-Cur-m-PNPs (1 mg/mL). Green and red fluorescence indicate live and dead cells, respectively. (b) Annexin V-FITC/PI fluorescence staining shows apoptosis/necrosis of T98G cells after 72 h incubation with 1 mg/mL Cur-m-PNPs or GRGDS-Cur-m-PNPs treatment (Annexin V-FITC green and PI red fluorescence).

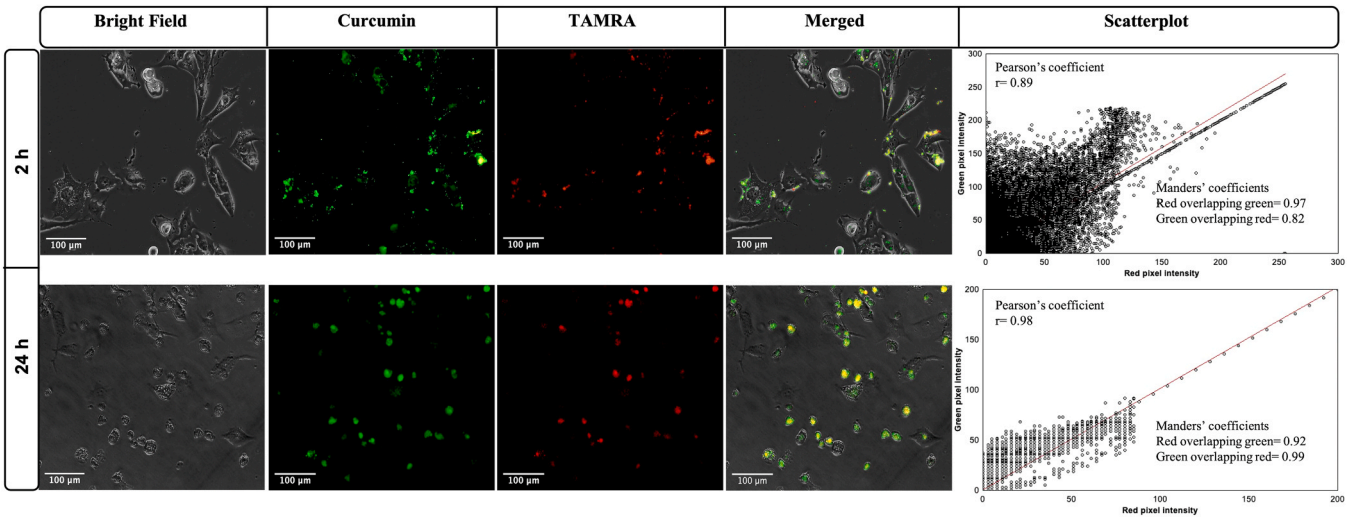

Fig. 8. Fluorescence images showing intracellular uptake of TAMRA-GRGDS-Cur-m-PNPs by T98G cells using curcumin (green) and TAMRA (red) fluorescent probes. 2.5×10^4 cells were seeded on the 24-well plate and incubated with 250 µg/mL TAMRA-GRGDS-Cur-m-PNPs (containing 4 µg/mL Cur) for 2 h and 24 h. After the incubation period, the cells were washed twice with PBS and imaged under fluorescence microscopy. Scatter plots of the colocalization of red and green fluorescent intensities were given on the rightmost panels.

Table 4
Concentrations of the Cur-m-PNPs and GRGDS-Cur-m-PNPs decided for the treatment of T98G cells for hyperthermia in the view of the loading and 24 h releasing amounts of Cur.

Parameters	Cur-m-PNPs	GRGDS-Cur-m-PNPs
µM Cur/mg NP	~200 µM	~40 µM
The dose of NP treated to T98G cells for hyperthermia	750 µg/mL	750 µg/mL
µM Cur/750 µg NP (hyperthermia concentration of NPs)	~150 µM	~30 µM
Cur release from NP in 24 h	~65 (from Fig. 3)	~60 (from Fig. 3)
The dose of NP treated to T98G cells for hyperthermia (by the amount of Cur loading and releasing for 24 h)	97.5 µM	18 µM

shown in Table 2.

RF-hyperthermia experiment was carried out with RF power of 150 W at the frequency of 13.56 MHz for 15 min exposure. During the hyperthermia, the rise in temperature of the cell culture medium was monitored by using a thermal camera (Fig. S6). Fig. S7 also shows the increase in temperature (ΔT) as a function of heating time (t). The increase in temperature of culture medium containing T98G cells treated with 750 µg/mL of m-PNPs, Cur-m-PNPs and GRGDS-Cur-m-PNPs were 6.1 °C, 5.8 °C and 5.9 °C; and also heating up to 43.0 °C, 43.2 °C and 43.5 °C, respectively. Thus, all kinds of NPs contributed to rising in temperature almost at the same level to the culture medium (~6 °C) and heating to ~43 °C. This can be explained by the fact that almost the same amount of iron was encapsulated in the nanoparticles for each sample group, based on the results from the iron content analysis (~25 µg Fe/1 mg PLGA). On the other hand, the NPs free culture medium (control) displayed about a 2.5 °C rise in temperature induced by RF-hyperthermia. During the RF-hyperthermia, the rise in temperature of the NPs free medium may be associated with electrical conductivity

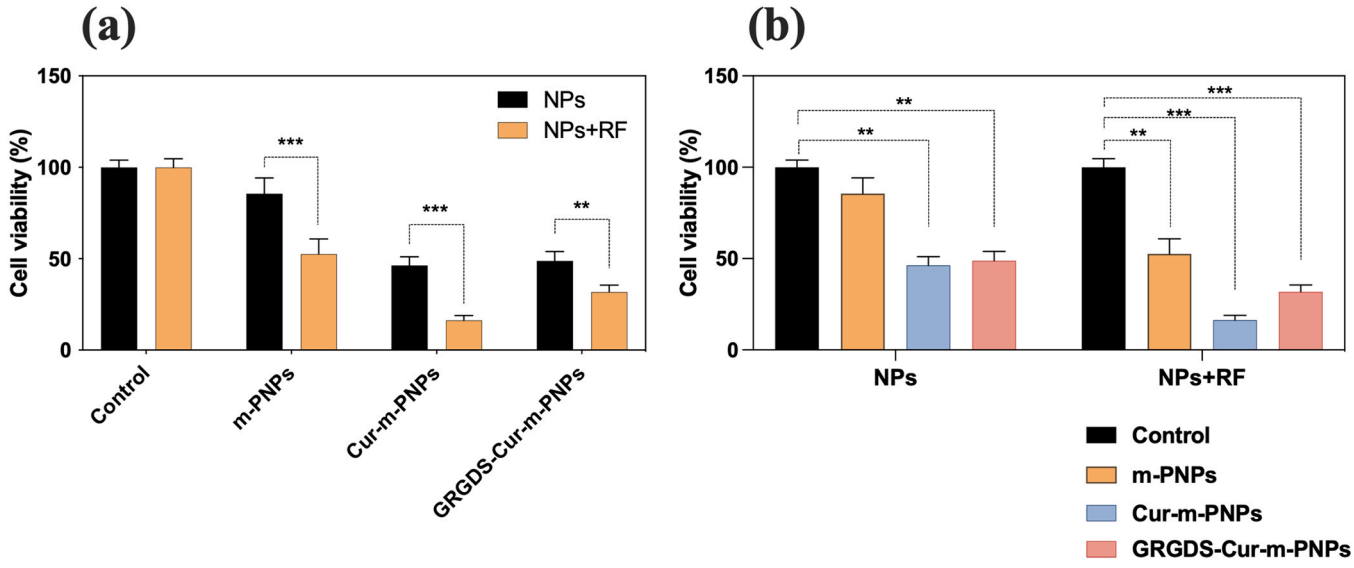

Fig. 9. *In vitro* cytotoxicity of different NPs and NPs+RF treatment on T98G cells. Cell viability was performed by MTT assay. Values represent mean ± SD (n = 5), $^*p \leq 0.05$, $^{**}p \leq 0.01$, $^{***}p \leq 0.001$.

caused by electrolytes contained in the cell culture medium [75]. Also, another reason could be the capacitive effect of two consecutive coil windings and the resulting undesirable stray electrical fields which can create hot spots [76]. Minaei et al. designed temozolomide-loaded folic acid-functionalized magnetic polymeric NPs to investigate anticancer efficiency on C6 glioblastoma cancer cells with RF-field exposure (13.56 MHz, 80 W). The rise in temperature of the culture medium containing C6 cells under 10 min RF exposure was measured as ~15 °C and ~9 °C in the presence and absence of NPs, respectively [77].

The effects of m-PNPs, Cur-m-PNPs and GRGDS-Cur-m-PNPs on the viability of T98G cells with or without RF-hyperthermia were determined by MTT analysis (Fig. 8). In the absence of RF-field, Cur-m-PNPs (non-targeted) and GRGDS-Cur-m-PNPs (targeted) have a similar cytotoxic effect on cells (Fig. 9b), and also both NPs significantly decreased cell viability compared to control cells ($p < 0.01$). After RF-field was applied, Cur-m-PNPs reduced cell viability (16%, $p < 0.001$) more than GRGDS-Cur-m-PNPs (31%, $p < 0.001$) (Fig. 9b). The reason for this may be related to Cur, which is not taken into the cells sufficiently in Cur-m-PNPs (non-targeted) without RF-field and has increased cellular uptake in the presence of RF-field. In other words, the hyperthermia-effect may have acted like GRGDS for cellular uptake. Several studies have been reported that the magnetic field increases cellular uptake and blood-brain barrier permeability [78,79]. The MTT results in the presence of NPs with or without RF-hyperthermia were further confirmed by the live/dead assay (Fig. 10a). After the RF-field was applied to the cells for 15 min, dead cells (stained red) were eliminated due to washing, trypsinization, and centrifugation process, so that only live cells (stained green) could be visualized using fluorescence microscopy. Fig. 10a showed the viable T98G cells after treatment with m-PNPs, Cur-m-PNPs or GRGDS-Cur-m-PNPs with or without RF-hyperthermia exposure. The cells treated with NPs and RF (NPs+RF) showed lower levels of cell viability as compared to the cells treated with only NPs. The live/dead assay finding is in good agreement with the results of the MTT assay.

Fig. 10b shows the Annexin V/PI fluorescence staining of T98G cells before and after RF treatment. As shown in Fig. 10b, very few dead cells were detected in the medium, and proliferation of T98G cells continued in both control groups of NPs and NPs+RF. However, the cells treated with NPs and RF-field underwent a higher level of cell death (especially

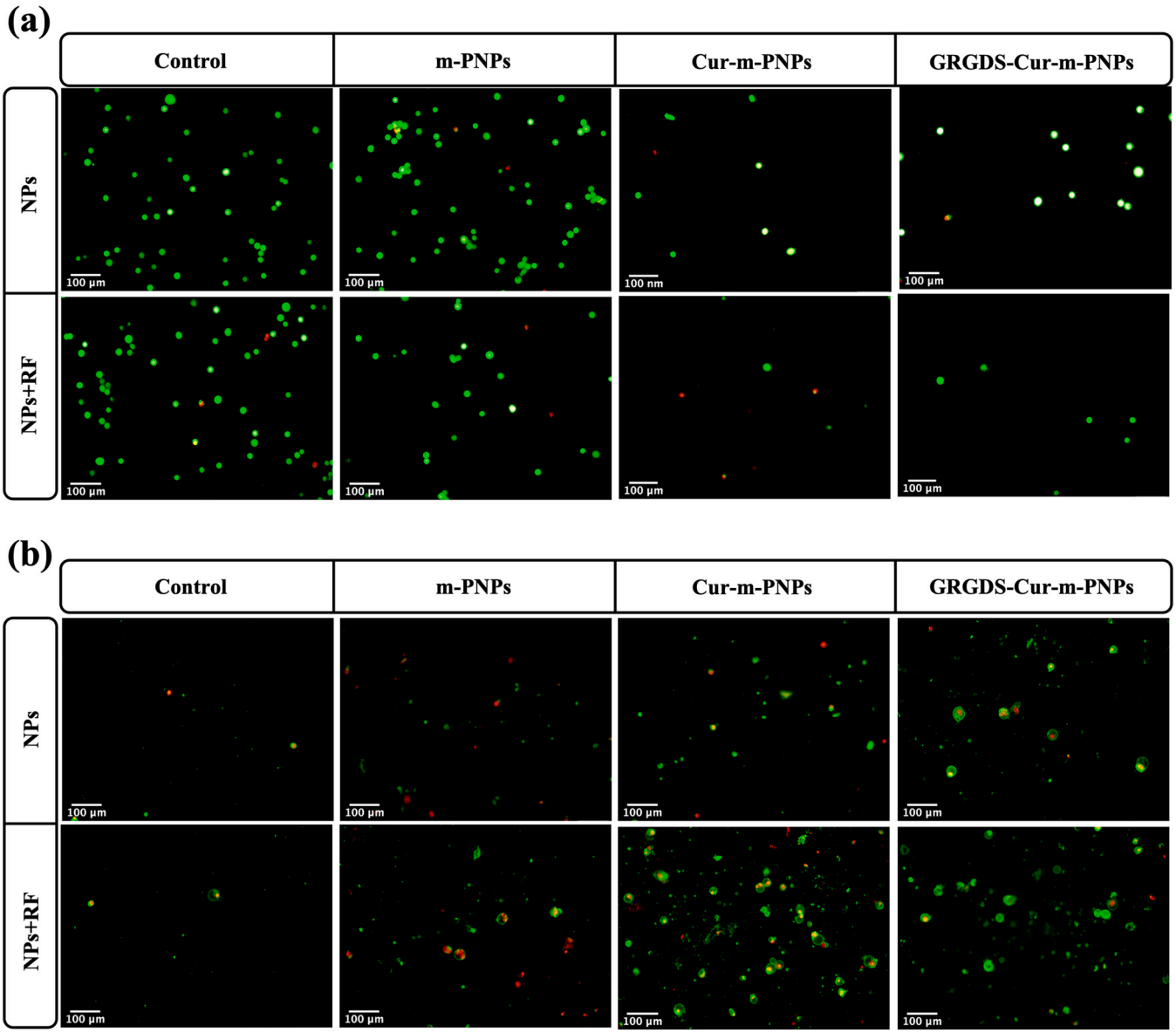

Fig. 10. (a) Live/dead analysis after NPs or NPs+RF treatment on T98G cells (20X), (b) Annexin V-PI staining after NPs or NPs+RF treatment on T98G cells (20X). Control groups for NPs and NPs+RF are only T98G cells incubated at the same conditions.

in the early apoptotic stage-Annexin V-FITC^{+}/PI^{-}) as compared to treated NPs. An increase in the number of necrotic cells was also observed in T98G cells treated with Cur-m-PNPs and RF, which likely represent late apoptotic cells (Annexin V-FITC^{+}/PI^{+}). Furthermore, the early apoptotic stage indicating intact cell membrane was more frequently observed in targeted NPs (GRGDS-Cur-m-PNPs) under RF-field. Our results are consistent with previous studies which outlined that curcumin treatment inhibits cellular proliferation and induces apoptosis in many cancer cells [3,80].

4. Conclusion

In this work, a portable RF-hyperthermia system was successfully implemented and tested that produces 400 W of RF output at 13.56 MHz for *in vitro* studies. This system was then combined with the multifunctional magnetic polymeric nanoparticles carrying a targeting ligand, GRGDS, to improve the therapeutic efficacy of a cytotoxic drug, curcumin, on GBM cells. The designed magnetic nanoparticles can release ~70% of their curcumin load during 72 h in a controlled manner while they show a heating performance sufficient to increase the temperature of T98G cells' environment to the hyperthermia temperature (43 °C) within 15 min. In addition to that, as prepared GRGDS-Cur-m-PNPs resulted the decrease of curcumin's therapeutic dose 2.5-fold (~15 μM) compared to free Cur (36 μM) and 6-fold relative to Cur-m-PNPs (~90 μM). Hence, we can say that GRGDS conjugation increased cellular uptake of the nanoparticles by specifically binding to cell receptors, thereby enhancing the bioavailability of curcumin. In the hyperthermia study, all NP groups showed toxicity to T98G cells with cell viability less than 50%, but the presence of curcumin reduced cell viability to 16% for Cur-m-PNPs and 31% for GRGDS-Cur-m-PNPs. Interestingly, Cur-m-PNPs showed more anti-proliferative effects than that of GRGDS-Cur-m-PNPs after hyperthermia exposure, indicating that hyperthermia may have also contributed to the increased cellular uptake *via* non-thermal effect. Overall, our data show a feasible approach of using the GRGDS-Cur-m-PNPs for RF-hyperthermia by the targeting delivery of Cur into glioblastoma cells.

CRediT authorship contribution statement

Fatih Senturk: Conceptualization, Methodology, Validation, Formal Analysis, Investigation, Data Curation, Writing – Original Draft, Visualization. **Soner Cakmak:** Conceptualization, Methodology, Investigation, Writing – Review&Editing, Supervision. **Ismail Cengiz Kocum:** Conceptualization, Methodology. **Menemse Gumusderelioglu:** Conceptualization, Resources, Writing – Review&Editing. **Goknur Guler Ozturk:** Conceptualization, Project Administration, Funding Acquisition.

Declaration of Competing Interest

The authors declare that they have no known competing financial interests or personal relationships that could have appeared to influence the work reported in this paper.

Acknowledgements

This study was supported by the Scientific and Technological Research Council of Turkey (TUBITAK), Grant no: SBAG-118S027 and SBAG-119S137. We are sincerely grateful for the assistance of the Cell and Tissue Engineering Research Group at Hacettepe University. We are also thankful to Dr. Anıl Sera Cakmak for the support of cell culture studies.

Appendix A. Supporting information

Supplementary data associated with this article can be found in the online version at doi:10.1016/j.colsurfa.2021.126648.

References

[1] S. Lapointe, A. Perry, N.A. Butowski, Primary brain tumours in adults, Lancet 392 (2018) 432–446.
[2] S. Pinel, N. Thomas, C. Boura, M. Barberi-Heyob, Approaches to physical stimulation of metallic nanoparticles for glioblastoma treatment, Adv. Drug Deliv. Rev. 138 (2019) 344–357.
[3] G. Jia, Y. Han, Y. An, Y. Ding, C. He, X. Wang, Q. Tang, NRP-1 targeted and cargo-loaded exosomes facilitate simultaneous imaging and therapy of glioma in vitro and in vivo, Biomaterials 178 (2018) 302–316.
[4] S. Quader, X. Liu, Y. Chen, P. Mi, T. Chida, T. Ishii, Y. Miura, N. Nishiyama, H. Cabral, K. Kataoka, cRGD peptide-installed epirubicin-loaded polymeric micelles for effective targeted therapy against brain tumors, J. Control. Rel. 258 (2017) 56–66.
[5] J. Aparicio-Blanco, L. Sanz-Arriazu, R. Lorenzoni, M.J. Blanco-Prieto, Glioblastoma chemotherapeutic agents used in the clinical setting and in clinical trials: nanomedicine approaches to improve their efficacy, Int. J. Pharm. 581 (2020), 119283.
[6] L. Berkelmann, A. Bader, S. Meshksar, A. Dierks, G. Hatipoglu Majernik, J. K. Krauss, K. Schwabe, D. Manteuffel, A. Ngezahayo, Tumour-treating fields (TTFields): Investigations on the mechanism of action by electromagnetic exposure of cells in telophase/cytokinesis, Sci. Rep. 9 (2019) 7362.
[7] P. Zhu, J.J. Zhu, Tumor treating fields: a novel and effective therapy for glioblastoma: mechanism, efficacy, safety and future perspectives, Chin. Clin. Oncol. 6 (2017) 41.
[8] R. Stupp, S. Taillibert, A. Kanner, W. Read, D. Steinberg, B. Lhermitte, S. Toms, A. Idbaih, M.S. Ahluwalia, K. Fink, F. Di Meco, F. Lieberman, J.J. Zhu, G. Stragliotto, D. Tran, S. Brem, A. Hottinger, E.D. Kirson, G. Lavy-Shahaf, U. Weinberg, C.Y. Kim, S.H. Paek, G. Nicholas, J. Bruna, H. Hirte, M. Weller, Y. Palti, M.E. Hegi, Z. Ram, Effect of tumor-treating fields plus maintenance temozolomide vs maintenance temozolomide alone on survival in patients with glioblastoma: a randomized clinical trial, J. Am. Med. Assoc. 318 (2017) 2306–2316.
[9] C. Prieto, I. Linares, Nanoparticles and nanothermia for malignant brain tumors, a suggestion of treatment for further investigations, Rep. Pract. Oncol. Radiother. 23 (2018) 474–480.
[10] H.A. Albarqi, L.H. Wong, C. Schumann, F.Y. Sabei, T. Korzun, X. Li, M.N. Hansen, P. Dhagat, A.S. Moses, O. Taratula, O. Taratula, Biocompatible nanoclusters with high heating efficiency for systemically delivered magnetic hyperthermia, ACS Nano 13 (2019) 6383–6395.
[11] Q. Zhou, Y. Wang, J. Xiao, H. Fan, Fabrication and characterisation of magnetic graphene oxide incorporated Fe_3O_4@ polyaniline for the removal of bisphenol A, t-octyl-phenol, and α-naphthol from water, Sci. Rep. 7 (2017) 1–11.
[12] A. Jozefczak, K. Kaczmarek, T. Hornowski, M. Kubovcikova, Z. Rozynek, M. Timko, A. Skumiel, Magnetic nanoparticles for enhancing the effectiveness of ultrasonic hyperthermia, Appl. Phys. Lett. 108 (2016), 263701.
[13] P.-O. Champagne, H. Westwick, A. Bouthillier, M. Sawan, Colloidal stability of superparamagnetic iron oxide nanoparticles in the central nervous system: a review, Nanomedicine 13 (2018) 1385–1400.
[14] S.M. Dadfar, K. Roemhild, N.I. Drude, S. von Stillfried, R. Knuchel, F. Kiessling, T. Lammers, Iron oxide nanoparticles: diagnostic, therapeutic and theranostic applications, Adv. Drug Deliv. Rev. 138 (2019) 302–325.
[15] M. Neamtu, C. Nadejde, V.-D. Hodoroaba, R.J. Schneider, L. Verestiuc, U. Panne, Functionalized magnetic nanoparticles: synthesis, characterization, catalytic application and assessment of toxicity, Sci. Rep. 8 (2018) 1–11.
[16] Y.M. Tsai, C.F. Chien, L.C. Lin, T.H. Tsai, Curcumin and its nano-formulation: the kinetics of tissue distribution and blood-brain barrier penetration, Int. J. Pharm. 416 (2011) 331–338.
[17] P.M. Luthra, N. Lal, Prospective of curcumin, a pleiotropic signalling molecule from Curcuma longa in the treatment of Glioblastoma, Eur. J. Med. Chem. 109 (2016) 23–35.
[18] A. Zanotto-Filho, E. Braganhol, K. Klafke, F. Figueiro, S.R. Terra, F.J. Paludo, M. Morrone, I.J. Bristot, A.M. Battastini, C.M. Forcelini, A.J.R. Bishop, D.P. Gelain, J.C.F. Moreira, Autophagy inhibition improves the efficacy of curcumin/temozolomide combination therapy in glioblastomas, Cancer Lett. 358 (2015) 220–231.
[19] Y. Li, Q. Zou, C. Yuan, S. Li, R. Xing, X. Yan, Amino acid coordination driven self-assembly for enhancing both the biological stability and tumor accumulation of curcumin, Angew. Chem. Int. Ed. 57 (2018) 17084–17088.
[20] A. Umapathi, P. Navya, H. Madhyastha, M. Singh, R. Madhyastha, M. Maruyama, H.K. Daima, Curcumin and isonicotinic acid hydrazide functionalized gold nanoparticles for selective anticancer action, Colloids Surf. A Physicochem. Eng. Asp. 607 (2020), 125484.
[21] S.-C. Hong, K.-M. Park, C.R. Hong, J.-C. Kim, S.-H. Yang, H.-S. Yu, H.-D. Paik, C.-H. Pan, P.-S. Chang, Microfluidic assembly of liposomes dual-loaded with catechin and curcumin for enhancing bioavailability, Colloids Surf. A Physicochem. Eng. Asp. 594 (2020), 124670.
[22] D. Prado-Audelo, L. María, I.H. Caballero-Florán, J.A. Meza-Toledo, N. Mendoza-Muñoz, M. González-Torres, B. Florán, H. Cortés, G. Leyva-Gómez, Formulations of curcumin nanoparticles for brain diseases, Biomolecules 9 (2019) 56.
[23] J.S. Ananta, R. Paulmurugan, T.F. Massoud, Temozolomide-loaded PLGA nanoparticles to treat glioblastoma cells: a biophysical and cell culture evaluation, Neurol. Res. 38 (2016) 51–59.

[24] D.R. Perinelli, M. Cespi, G. Bonacucina, G.F. Palmieri, PEGylated polylactide (PLA) and poly (lactic-co-glycolic acid) (PLGA) copolymers for the design of drug delivery systems, J. Pharm. Investig. 49 (2019) 443–458.
[25] W. Rao, W. Zhang, I. Poventud-Fuentes, Y. Wang, Y. Lei, P. Agarwal, B. Weekes, C. Li, X. Lu, J. Yu, X. He, Thermally responsive nanoparticle-encapsulated curcumin and its combination with mild hyperthermia for enhanced cancer cell destruction, Acta Biomater. 10 (2014) 831–842.
[26] M.M. Patel, B.M. Patel, Crossing the blood-brain barrier: recent advances in drug delivery to the brain, CNS Drugs 31 (2017) 109–133.
[27] D. Duan, A. Wang, L. Ni, L. Zhang, X. Yan, Y. Jiang, H. Mu, Z. Wu, K. Sun, Y. Li, Trastuzumab- and Fab' fragment-modified curcumin PEG-PLGA nanoparticles: preparation and evaluation in vitro and in vivo, Int. J. Nanomed. 13 (2018) 1831–1840.
[28] A. Montazerabadi, J. Beik, R. Irajirad, N. Attaran, S. Khaledi, H. Ghaznavi, A. Shakeri-Zadeh, Folate-modified and curcumin-loaded dendritic magnetite nanocarriers for the targeted thermo-chemotherapy of cancer cells, Artif. Cells Nanomed. Biotechnol. 47 (2019) 330–340.
[29] L. Zhao, C. Yang, J. Dou, Y. Xi, H. Lou, G. Zhai, Development of RGD-functionalized PEG-PLA micelles for delivery of curcumin, J. Biomed. Nanotechnol. 11 (2015) 436–446.
[30] N.H. Abd Ellah, S.A. Abouelmagd, Surface functionalization of polymeric nanoparticles for tumor drug delivery: approaches and challenges, Expert Opin. Drug Deliv. 14 (2017) 201–214.
[31] S.-Y. Li, L.-H. Liu, H.-Z. Jia, W.-X. Qiu, L. Rong, H. Cheng, X.-Z. Zhang, A. pH-responsive, prodrug for real-time drug release monitoring and targeted cancer therapy, Chem. Commun. 50 (2014) 11852–11855.
[32] Y. Miura, T. Takenaka, K. Toh, S. Wu, H. Nishihara, M.R. Kano, Y. Ino, T. Nomoto, Y. Matsumoto, H. Koyama, Cyclic RGD-linked polymeric micelles for targeted delivery of platinum anticancer drugs to glioblastoma through the blood–brain tumor barrier, ACS Nano 7 (2013) 8583–8592.
[33] A. Hardiansyah, M.C. Yang, T.Y. Liu, C.Y. Kuo, L.Y. Huang, T.Y. Chan, Hydrophobic drug-loaded pegylated magnetic liposomes for drug-controlled release, Nanoscale Res. Lett. 12 (2017) 355.
[34] M.M. Yallapu, S.F. Othman, E.T. Curtis, B.K. Gupta, M. Jaggi, S.C. Chauhan, Multi-functional magnetic nanoparticles for magnetic resonance imaging and cancer therapy, Biomaterials 32 (2011) 1890–1905.
[35] A.A. Allam, M.E. Sadat, S.J. Potter, D.B. Mast, D.F. Mohamed, F.S. Habib, G. M. Pauletti, Stability and magnetically induced heating behavior of lipid-coated Fe_3O_4 nanoparticles, Nanoscale Res. Lett. 8 (2013) 426.
[36] N.S. Rejinold, R.G. Thomas, M. Muthiah, H.J. Lee, Y.Y. Jeong, I.K. Park, R. Jayakumar, Breast tumor targetable Fe_3O_4 embedded thermo-responsive nanoparticles for radiofrequency assisted drug delivery, J. Biomed. Nanotechnol. 12 (2016) 43–55.
[37] L. Huerta-Nuñez, G. Gutierrez-Iglesias, A. Martinez-Cuazitl, M. Mata-Miranda, V. Alvarez-Jiménez, V. Sánchez-Monroy, A. Golberg, C. González-Díaz, A biosensor capable of identifying low quantities of breast cancer cells by electrical impedance spectroscopy, Sci. Rep. 9 (2019) 1–12.
[38] P. Wust, B. Kortüm, U. Strauss, J. Nadobny, S. Zschaeck, M. Beck, U. Stein, P. Ghadjar, Non-thermal effects of radiofrequency electromagnetic fields, Sci. Rep. 10 (2020) 1–8.
[39] G. Andocs, M. Rehman, Q. Zhao, Y. Tabuchi, M. Kanamori, T. Kondo, Comparison of biological effects of modulated electro-hyperthermia and conventional heat treatment in human lymphoma U937 cells, Cell Death Discov. 2 (2016) 1–10.
[40] C.-C. Chen, C.-L. Chen, J.-J. Li, Y.-Y. Chen, C.-Y. Wang, Y.-S. Wang, K.-H. Chi, H.-E. Wang, Presence of gold nanoparticles in cells associated with the cell-killing effect of modulated electro-hyperthermia, ACS Appl. Bio Mater. 2 (2019) 3573–3581.
[41] J. Park, K. An, Y. Hwang, J.G. Park, H.J. Noh, J.Y. Kim, J.H. Park, N.M. Hwang, T. Hyeon, Ultra-large-scale syntheses of monodisperse nanocrystals, Nat. Mater. 3 (2004) 891–895.
[42] S. Prabhu, J.S. Goda, S. Mutalik, B.S. Mohanty, P. Chaudhari, S. Rai, N. Udupa, B.S. S. Rao, A polymeric temozolomide nanocomposite against orthotopic glioblastoma xenograft: tumor-specific homing directed by nestin, Nanoscale 9 (2017) 10919–10932.
[43] H. Chun, S.W. Shin, L. Amornkitbamrung, S.Y. Ahn, J.S. Yuk, S.J. Sim, D. Luo, S. H. Um, Polymeric nanocomplex encapsulating iron oxide nanoparticles in constant size for controllable magnetic field reactivity, Langmuir 34 (2018) 12827–12833.
[44] W. Elsayed, F.S. Al-Hazmi, L.S. Memesh, L.M. Bronstein, A novel approach for rapid green synthesis of nearly mono-disperse iron oxide magnetic nanocubes with remarkable surface magnetic anisotropy density for enhancing hyperthermia performance, Colloids Surf. A Physicochem. Eng. Asp. 529 (2017) 239–245.
[45] F. Senturk, S. Çakmak, G.G. Ozturk, Synthesis and characterization of oleic acid coated magnetic nanoparticles for hyperthermia applications, Nat. Appl. Sci. J. 2 (2019) 16–29.
[46] W. Yang, F.X. Song, S. Wang, L. Zhang, X. Zeng, Y. Li, Multifunctional mesoporous silica nanoparticles with different morphological characteristics for in vitro cancer treatment, Colloids Surf. A Physicochem. Eng. Asp. 610 (2021), 125717.
[47] C. Kutlu, A.S. Cakmak, M. Gümüşderelioğlu, Double-effective chitosan scaffold-PLGA nanoparticle system for brain tumour therapy: in vitro study, J. Microencapsul. 31 (2014) 700–707.
[48] K.W. Dunn, M.M. Kamocka, J.H. McDonald, A practical guide to evaluating colocalization in biological microscopy, Am. J. Physiol. Cell Physiol. 300 (2011) C723–C742.
[49] A. Rajan, N.K. Sahu, Inductive calorimetric assessment of iron oxide nano-octahedrons for magnetic fluid hyperthermia, Colloids Surf. A Physicochem. Eng. Asp. 603 (2020), 125210.
[50] J. Ibarra, J. Melendres, M. Almada, M.G. Burboa, P. Taboada, J. Juárez, M. A. Valdez, Synthesis and characterization of magnetite/PLGA/chitosan nanoparticles, Mater. Res. Express 2 (2015), 095010.
[51] M. Darwish, U. Kunz, U. Peuker, Preparation and catalytic use of platinum in magnetic core/shell nanocomposites, J. Appl. Polym. Sci. 129 (2013) 1806–1811.
[52] G.A. El-Mahdy, A.M. Atta, H.A. Al-Lohedan, Synthesis and evaluation of poly (sodium 2-acrylamido-2-methylpropane sulfonate-co-styrene)/magnetite nanoparticle composites as corrosion inhibitors for steel, Molecules 19 (2014) 1713–1731.
[53] Y.H. Lee, D.S. Chang, Fabrication, characterization, and biological evaluation of anti-HER2 indocyanine green-doxorubicin-encapsulated PEG-b-PLGA copolymeric nanoparticles for targeted photochemotherapy of breast cancer cells, Sci. Rep. 7 (2017) 46688.
[54] H. Fasehee, R. Dinarvand, A. Ghavamzadeh, M. Esfandyari-Manesh, H. Moradian, S. Faghihi, S.H. Ghaffari, Delivery of disulfiram into breast cancer cells using folate-receptor-targeted PLGA-PEG nanoparticles: in vitro and in vivo investigations, J. Nanobiotechnol. 14 (2016) 32.
[55] S.M. Solyman, M.S. Darwish, J. Yoon, Catalytic activity of hybrid iron oxide silver nanoparticles in methyl methacrylate polymerization, Catalysts 10 (2020) 422.
[56] A. Spivakov, C.-R. Lin, Y.-C. Chang, C.-C. Wang, D. Sarychen, Magnetic and magneto-optical oroperties of iron oxides nanoparticles synthesized under atmospheric pressure, Nanomaterials 10 (2020) 1888.
[57] E.D. Smolensky, H.-Y.E. Park, Y. Zhou, G.A. Rolla, M. Marjanska, M. Botta, V. C. Pierre, Scaling laws at the nanosize: the effect of particle size and shape on the magnetism and relaxivity of iron oxide nanoparticle contrast agent, J. Mater. Chem. B 1 (2013) 2818–2828.
[58] K. Wu, D. Su, J. Liu, R. Saha, J.-P. Wang, Magnetic nanoparticles in nanomedicine: a review of recent advances, Nanotechnology 30 (2019), 502003.
[59] C. Nehate, M.R.A. Alex, A. Kumar, V. Koul, Combinatorial delivery of superparamagnetic iron oxide nanoparticles (γFe2O3) and doxorubicin using folate conjugated redox sensitive multiblock polymeric nanocarriers for enhancing the chemotherapeutic efficacy in cancer cells, Mater. Sci. Eng. C Mater. Biol. Appl. 75 (2017) 1128–1143.
[60] S. Ayyanaar, M.P. Kesavan, G. Sivaraman, B. Maddiboyina, J. Annaraj, J. Rajesh, G. Rajagopal, A novel curcumin-loaded PLGA micromagnetic composite system for controlled and pH-responsive drug delivery, Colloids Surf. A Physicochem. Eng. Asp. 573 (2019) 188–195.
[61] Z. Jamali, M. Khoobi, S.M. Hejazi, N. Eivazi, S. Abdolahpour, F. Imanparast, H. Moradi-Sardareh, M. Paknejad, Evaluation of targeted curcumin (CUR) loaded PLGA nanoparticles for in vitro photodynamic therapy on human glioblastoma cell line, Photodaign. Photodyn. Ther. 23 (2018) 190–201.
[62] S. Doggui, J.K. Sahni, M. Arseneault, L. Dao, C. Ramassamy, Neuronal uptake and neuroprotective effect of curcumin-loaded PLGA nanoparticles on the human SK-N-SH cell line, J. Alzheimers Dis. 30 (2012) 377–392.
[63] Z.A. Busari, K.A. Dauda, O.A. Morenikeji, F. Afolayan, O.T. Oyeyemi, J. Meena, D. Sahu, A.K. Panda, Antiplasmodial activity and toxicological assessment of curcumin PLGA-encapsulated nanoparticles, Front. Pharmacol. 8 (2017) 622.
[64] J. Yoo, Y.-Y. Won, Phenomenology of the initial burst release of drugs from PLGA microparticles, ACS Biomater. Sci. Eng. 6 (2020) 6053–6062.
[65] T. Higuchi, Mechanism of sustained-action medication. Theoretical analysis of rate of release of solid drugs dispersed in solid matrices, J. Pharm. Sci. 52 (1963) 1145–1149.
[66] R.W. Korsmeyer, R. Gurny, E. Doelker, P. Buri, N.A. Peppas, Mechanisms of solute release from porous hydrophilic polymers, Int. J. Pharm. 15 (1983) 25–35.
[67] M.H. Asfour, A.M. Mohsen, Formulation and evaluation of pH-sensitive rutin nanospheres against colon carcinoma using HCT-116 cell line, J. Adv. Res. 9 (2018) 17–26.
[68] P. Langone, P.R. Debata, R. Inigo Jdel, S. Dolai, S. Mukherjee, P. Halat, K. Mastroianni, G.M. Curcio, M.R. Castellanos, K. Raja, P. Banerjee, Coupling to a glioblastoma-directed antibody potentiates antitumor activity of curcumin, Int. J. Cancer 135 (2014) 710–719.
[69] S. Karmakar, N.L. Banik, S.J. Patel, S.K. Ray, Curcumin activated both receptor-mediated and mitochondria-mediated proteolytic pathways for apoptosis in human glioblastoma T98G cells, Neurosci. Lett. 407 (2006) 53–58.
[70] F. Dilnawaz, S.K. Sahoo, Enhanced accumulation of curcumin and temozolomide loaded magnetic nanoparticles executes profound cytotoxic effect in glioblastoma spheroid model, Eur. J. Pharm. Biopharm. 85 (2013) 452–462.
[71] K. Jiang, M. Shen, W. Xu, Arginine, glycine, aspartic acid peptide-modified paclitaxel and curcumin co-loaded liposome for the treatment of lung cancer: in vitro/vivo evaluation, Int. J. Nanomed. 13 (2018) 2561–2569.
[72] K. Kaur, V. Prabha, Impairment by sperm agglutinating factor isolated from Escherichia coli: receptor specific interactions, BioMed. Res. Int. 2013 (2013), 548497.

[73] E. Brauchle, S. Thude, S.Y. Brucker, K. Schenke-Layland, Cell death stages in single apoptotic and necrotic cells monitored by Raman microspectroscopy, Sci. Rep. 4 (2014) 4698.
[74] A.S. Wadajkar, Z. Bhavsar, C.-Y. Ko, B. Koppolu, W. Cui, L. Tang, K.T. Nguyen, Multifunctional particles for melanoma-targeted drug delivery, Acta Biomater. 8 (2012) 2996–3004.
[75] A. Goldman, AC Properties of Ferrites. Modern Ferrite Technology, 2006, pp. 35–50.
[76] M. Mehdizadeh, Microwave/RF applicators and probes: for material heating, sensing, and plasma generation, William Andrew 2015.
[77] S.E. Minaei, S. Khoei, S. Khoee, F. Vafashoar, V.P. Mahabadi, In vitro anti-cancer efficacy of multi-functionalized magnetite nanoparticles combining alternating magnetic hyperthermia in glioblastoma cancer cells, Mater. Sci. Eng. C Mater. Biol. Appl. 101 (2019) 575–587.
[78] F. D'Agata, F.A. Ruffinatti, S. Boschi, I. Stura, I. Rainero, O. Abollino, R. Cavalli, C. Guiot, Magnetic nanoparticles in the central nervous system: targeting principles, applications and safety issues, Molecules 23 (2018) 9.
[79] Q. He, J. Liu, J. Liang, X. Liu, W. Li, Z. Liu, Z. Ding, D. Tuo, Towards improvements for penetrating the blood–brain barrier—recent progress from a material and pharmaceutical perspective, Cells 7 (2018) 24.
[80] M.M. Yallapu, S.F. Othman, E.T. Curtis, N.A. Bauer, N. Chauhan, D. Kumar, M. Jaggi, S.C. Chauhan, Curcumin-loaded magnetic nanoparticles for breast cancer therapeutics and imaging applications, Int. J. Nanomed. 7 (2012) 1761–1779.